PTEP

Prog. Theor. Exp. Phys. **2023** 113J01(36 pages)
DOI: 10.1093/ptep/ptad126

Rheology of a dilute binary mixture of inertial suspension under simple shear flow

Satoshi Takada [1,*], Hisao Hayakawa [2,*], and Vicente Garzó [3,*]

[1] *Institute of Engineering and Department of Mechanical Systems Engineering, Tokyo University of Agriculture and Technology, 2-24-16, Naka-cho, Koganei, Tokyo 184–8588, Japan*
[2] *Yukawa Institute for Theoretical Physics, Kyoto University, Kitashirakawa Oiwakecho, Sakyo-ku, Kyoto 606–8502, Japan*
[3] *Departamento de Física and Instituto de Computación Científica Avanzada (ICCAEX), Universidad de Extremadura, E-06006 Badajoz, Spain*
*E-mail: takada@go.tuat.ac.jp, hisao@yukawa.kyoto-u.ac.jp, vicenteg@unex.es

Received May 11, 2023; Revised September 1, 2023; Accepted October 4, 2023; Published October 5, 2023

The rheology of a dilute binary mixture of inertial suspension under simple shear flow is analyzed in the context of the Boltzmann kinetic equation. The effect of the surrounding viscous gas on the solid particles is accounted for by means of a deterministic viscous drag force plus a stochastic Langevin-like term defined in terms of the environmental temperature $T_{\rm env}$. Grad's moment method is employed to determine the temperature ratio and the pressure tensor in terms of the coefficients of restitution, concentration, the masses and diameters of the components of the mixture, and the environmental temperature. Analytical results are compared against event-driven Langevin simulations for mixtures of hard spheres with the same mass density $m_1/m_2 = (\sigma^{(1)}/\sigma^{(2)})^3$, m_i and $\sigma^{(1)}$ being the mass and diameter, respectively, of the species i. It is confirmed that the theoretical predictions agree with simulations of various size ratios $\sigma^{(1)}/\sigma^{(2)}$ and for elastic and inelastic collisions in a wide range of parameter space. It is remarkable that the temperature ratio T_1/T_2 and the viscosity ratio η_1/η_2 (η_i being the partial contribution of the species i to the total shear viscosity $\eta = \eta_1 + \eta_2$) discontinuously change at a certain shear rate as the size ratio increases; this feature (which is expected to occur in the thermodynamic limit) cannot be completely captured by simulations due to the small system size. In addition, a Bhatnagar–Gross–Krook (BGK)-type kinetic model adapted to mixtures of inelastic hard spheres is exactly solved when $T_{\rm env}$ is much smaller than the kinetic temperature T. A comparison between the velocity distribution functions obtained from Grad's method, the BGK model, and simulations is carried out.

Subject Index A57, J01, J44

1. Introduction

Rheology is the study of the flow properties of materials. Although the viscosity of a Newtonian fluid is independent of the shear rate, there are many domestic substances (liquids containing microstructures such as suspensions and polymers) where the viscosity depends on the shear rate (non-Newtonian fluids). Within the class of non-Newtonian fluids, some of them exhibit shear thinning (namely, when the viscosity *decreases* with the shear rate) while others display shear thickening (namely, when the viscosity *increases* with the shear rate). The shear thickening is also categorized into two classes, continuous shear thickening (CST) and discontinuous shear thickening (DST). The viscosity increases continuously in CST, while it abruptly changes discontinuously from a small value to a large value at a critical shear rate in DST. DST has at-

tracted much attention among physicists in the last few years [1–7] as a typical nonequilibrium discontinuous phase transition between a liquid-like phase and a solid-like phase. In addition, the understanding of the origin of DST is also important for potential industrial applications such as protective vests and traction controls.

Although most of the previous studies on shear thickening have focused on dense suspensions, there are some other studies that analyze a DST-like process for the kinetic temperature of inertial suspensions. This type of inertial suspension can be regarded as an idealistic aerosol model [8]. The DST-like process (or the ignited–quenched transition) of dilute inertial suspensions takes place as a result of a saddle-node bifurcation. On the other hand, the DST-like process for dilute suspensions becomes CST-like as the density of suspensions increases [9–16].

To gain some insight into the understanding of the generic features of rheological phase transitions, we use kinetic theory tools in this paper. This allows us to offer a quantitative theoretical analysis for the DST-like and CST-like processes in inertial suspensions. However, it should be noted that some previous kinetic theories for inertial suspensions have ignored thermal fluctuations in the dynamics of grains [9–11,14]. A refined suspension model including a Langevin-like term has been more recently considered in Refs. [12,13,15–17]. The quantitative validity of these studies has already been verified by an event-driven Langevin simulation for hard spheres (EDLSHS) [15,16,18].

Most of the previous theoretical studies on the rheology of inertial suspensions have focused on monodisperse systems, namely, suspensions containing only identical spherical particles. In reality, suspended particles are not identical since the size of the particles is distributed and the shape and mechanical properties of the particles are also different. To quantify the impact of polydispersity on the rheological properties of inertial suspensions under simple or uniform shear flows (USF), we consider a binary mixture in this paper, namely, a suspension that contains two kinds of spherical particles having different sizes. We note that bidisperse systems are also studied in colloidal and blood suspensions [19–22].

A challenging and interesting problem in sheared granular binary mixtures is that of diffusion. It is well established that in the absence of shear the mass flux is proportional to the density, pressure, and temperature gradients where the corresponding transport coefficients are scalar quantities [23]. However, when the mixture is strongly sheared, due to the anisotropy induced by the shear flow, tensorial quantities are required to characterize the mass transport instead of the conventional scalar diffusion coefficients. There have been some previous attempts to describe the self-diffusion problem in sheared granular mixtures [24,25]. As expected, all previous studies indicate that the diffusion process in USF is highly anisotropic and the components of the diffusion can be observed in directions parallel and perpendicular to the velocity gradient. To characterize such anisotropy of the diffusion tensor, there have been several theoretical studies based on kinetic theory [26,27], simulations of rapid granular shear flows [28,29], and experimental studies of dense, granular shear flows in a 2D Couette geometry [30,31].

One of the key features of flows of polydisperse particles is segregation [32]. This is likely one of the most relevant problems in granular mixtures, from the practical and fundamental points of view. However, despite the industrial and scientific progress made in the past few years, the mechanisms involved in the segregation phenomenon are still poorly understood. In particular, in the context of kinetic theory, many different papers have addressed the study of segregation [33–42]. On the other hand, computer simulations of bidisperse granular mixtures under USF (and without any influence of gravity) [43] have not found any sign of large-scale

size segregation. Another type of work has studied segregation in flows down inclined slopes in which approximate simple shear flows have been realized, at least in the bulk regions away from the bottom boundaries and surfaces. It is remarkable that the trigger for segregation is the deviation from the USF of the velocity profile, as has been reported in Ref. [42]. This suggests that segregation can be observed even for dilute mixtures without the influence of gravity, if we drive a shear flow through a boundary. In other words, the segregation is localized near the boundaries.

Previous studies of granular binary mixtures based on the kinetic theory have mainly focused on obtaining the Navier–Stokes transport coefficients of the mixture by considering states close to the homogeneous cooling state [23] and/or close to driven stationary homogeneous states [44–46]. The results are scarcer in the study of the rheological properties of granular binary mixtures under USF [43,47–49]. As expected, the results show that the mixture is non-Newtonian and, in some cases, the effect of bidispersity enhances the non-Newtonian character of the fluid. Since the USF is spatially homogeneous in the frame moving with the linear velocity field, no segregation appears in the system. However, when the USF state is slightly perturbed by small density and temperature gradients, a nonvanishing mass flux is present and the corresponding components of the diffusion tensors have been determined in the tracer limit in Refs. [26,27]. The knowledge of the shear-rate dependence of the above diffusion tensors has allowed the analysis of thermal diffusion segregation induced by the presence of a temperature gradient orthogonal to the shear flow plane [50].

Nevertheless, so far and to the best of our knowledge, there are few studies of binary mixtures of inertial suspensions including diffusion processes, in which the rheology of inertial suspensions drastically depends on the shear rate. Thus, as already done in the case of granular mixtures [26,27], one has to determine the rheological properties of sheared binary mixtures of inertial suspensions as a first step before considering the segregation problem. Once the rheology is known, the components of the diffusion tensors can be determined by using a similar procedure to the one followed in (dry) granular mixtures. Therefore, the study of the rheology of a *dilute* binary mixture of inertial suspension is an important issue.

Beyond dilute granular flows, it is quite apparent that there are many exotic rheological processes in dense flows. These processes include glass transitions, shear jamming, jamming, and DST [1–7,51–54]. Such exotic processes cannot be observed in monodisperse systems but they can be observed only in mixtures when the volume fraction exceeds the transition point for crystallization of identical spheres at the volume fraction $\varphi = 0.49$.

In this paper, we focus on the rheology of a dilute binary mixture under USF. As in our previous work [15,16], the influence of the interstitial gas on solid particles is accounted for in an effective way by means of (i) a deterministic drag force proportional to the particle velocity and (ii) a stochastic Langevin-like term. While the first contribution attempts to model the friction of grains on the viscous fluid (a collection of gas molecules), the second term mimics the energy gained by the solid particles due to their interactions with the particles of the surrounding gas. The corresponding set of two coupled Boltzmann kinetic equations is solved by two complementary and independent routes: (i) Grad's moment method and (ii) event-driven simulations for hard spheres (EDLSHS). The comparison between kinetic theory and EDLSHS allows us to verify the reliability of the theoretical predictions as the first step to tackle the behavior of sheared binary mixtures of inertial suspensions. Our (approximate) analytical results of the rheological properties of the mixture (the ratio T_1/T_2 between the partial temperatures and the

pressure tensor) agree well with simulations for conditions of practical interest. In particular, the temperature ratio T_1/T_2 and the viscosity ratio η_1/η_2 (where η_i is the partial contribution of the component i to the total shear viscosity $\eta = \eta_1 + \eta_2$) exhibit a DST-like transition for sufficiently high values of the size ratio $\sigma^{(1)}/\sigma^{(2)}$. As a complement, we have also compared the velocity distribution function obtained by both Grad's moment method and a kinetic model with the one obtained by EDLSHS.

The contents of the paper are as follows. In Sect. 2, we introduce the Langevin model and Boltzmann equation for a binary mixture of inertial suspensions under a simple shear. Section 3 deals with the theoretical procedure to derive the rheology of inertial suspensions in USF. Section 4 is the main part of this paper, in which we present the theoretical and numerical results and find a new rheological phase transition similar to DST. The velocity distribution function is also studied by comparing the results from Grad's approximation and simulations. In Sect. 5, we discuss and conclude our results. Moreover, there are several appendices to explain the technical details of the paper. In Appendix A, the difference between $P_{yy}^{(i)}$ and $P_{zz}^{(i)}$ is discussed. In Appendix B, we provide some mathematical steps to compute the collisional moment needed to determine the components of the pressure tensor from Grad's method. The detailed rheological properties for the temperature ratio, temperature, and viscosity are discussed in Appendix C. Appendix D discusses how the discontinuous transition appears/disappears when we change the parameters of the mixture. The tracer limit of the theory is briefly presented in Appendix E while Appendix F gives the exact solution to a Bhatnagar–Gross–Krook (BGK)-like kinetic model for granular mixtures in the high-shear-rate regime. This solution provides a 2D velocity distribution function. Finally, the 1D velocity distribution function is displayed in Appendix G with a comparison with the one obtained from computer simulations.

2. Basic equations for a binary mixture of inertial suspension under uniform shear flows

In this section, we present the basic equations describing a dilute binary mixture of inertial suspensions under USF. In the first subsection, we introduce the Langevin equation characterizing the motion of each particle activated by the thermal noise caused by collisions with the environmental molecules. In the second subsection, we write the corresponding set of two coupled nonlinear Boltzmann kinetic equations for the bidisperse inertial suspension in the low-density regime.

2.1. *Langevin equation*

We consider a 3D binary mixture of inertial suspension modeled as a mixture of *inelastic* hard spheres of masses m_i and diameters $\sigma^{(i)}$ ($i = 1, 2$). For the sake of simplicity, we assume that the spheres are completely smooth and hence collisions among all pairs are characterized by (positive) constant coefficients of normal restitution $e_{ij} \leq 1$, where the subscripts ij denote the species i and j, respectively. Let us use the notations $\boldsymbol{v}_1^{(i)}$ and $\boldsymbol{v}_2^{(j)}$ when particle 1 (species i) collides with particle 2 (species j). The post-collisional velocities $\boldsymbol{v}_1^{(i)\prime}$ for particle 1 (species i) and $\boldsymbol{v}_2^{(j)\prime}$ for particle 2 (species j) are expressed as

$$\begin{cases} \boldsymbol{v}_1^{(i)\prime} = \boldsymbol{v}_1^{(i)} - \dfrac{m_{ij}}{m_i}\left(1+e_{ij}\right)\left(\boldsymbol{v}_{12}^{(ij)}\cdot\widehat{\boldsymbol{\sigma}}\right)\widehat{\boldsymbol{\sigma}}, \\ \boldsymbol{v}_2^{(j)\prime} = \boldsymbol{v}_2^{(j)} + \dfrac{m_{ij}}{m_j}\left(1+e_{ij}\right)\left(\boldsymbol{v}_{12}^{(ij)}\cdot\widehat{\boldsymbol{\sigma}}\right)\widehat{\boldsymbol{\sigma}}, \end{cases} \tag{1}$$

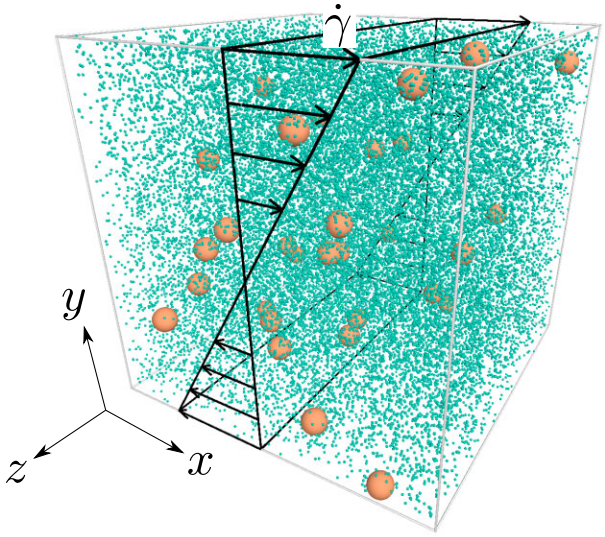

Fig. 1. Setup of our system. Two species of particles are distributed in a fluidized inertial suspension characterized by the temperature $T_{\rm env}$. The shear is applied with the shear rate $\dot{\gamma}$ in the xy plane, where the x and y axes are the shear direction and the velocity gradient direction, respectively. Here, we use $N = 30\,000$ particles with size and number ratios of $\sigma^{(1)}/\sigma^{(2)} = 10.0$ and $N_1/N_2 = 30/29\,970 = 1/999$, respectively.

where we have introduced the pre-collisional velocities of $\boldsymbol{v}_1^{(i)}$ for particles 1 (species i) and 2 (species j), $\boldsymbol{v}_{12}^{(ij)} \equiv \boldsymbol{v}_1^{(i)} - \boldsymbol{v}_2^{(j)}$, the unit normal vector at contact $\hat{\boldsymbol{\sigma}}$, and the reduced mass $m_{ij} \equiv m_i m_j/(m_i + m_j)$.

The inertial suspension that we consider is subjected to a steady simple shear flow in the x direction as shown in Fig. 1. The equation of motion for the kth particle of the species i is described by the Langevin equation

$$\frac{d\boldsymbol{p}_k^{(i)}}{dt} = -\zeta_i \boldsymbol{p}_k^{(i)} + \boldsymbol{F}_k^{\rm imp} + m_i \boldsymbol{\xi}_k^{(i)}, \tag{2}$$

where ζ_i is the drag coefficient acting on the particle of species i from the environmental fluid, and $\boldsymbol{p}_k^{(i)} \equiv m_i(\boldsymbol{v}_k^{(i)} - \dot{\gamma} y_k^{(i)} \boldsymbol{e}_x)$ is the peculiar momentum of the kth particle with velocity $\boldsymbol{v}_k^{(i)}$. Here, $\dot{\gamma}$ and $\boldsymbol{e}_x$ are the shear rate and unit vector in the sheared (x) direction, respectively. If hard-core grains are subjected to the Stokes' drag, ζ_i is simply proportional to $\sigma^{(i)}$ and $\sqrt{T_{\rm env}}$, where $T_{\rm env}$ is the environmental temperature. When we adopt the mean diameter $\overline{\sigma} \equiv (\sigma^{(1)} + \sigma^{(2)})/2$ and drag coefficient $\overline{\zeta} \equiv (\zeta_1 + \zeta_2)/2$, the coefficient ζ_i satisfies $\zeta_i/\overline{\zeta} \propto \sigma^{(i)}/\overline{\sigma}$. For denser flows, the dependence of ζ_i on the parameters of the mixture is more complex [55,56]. In Eq. (2), $\boldsymbol{F}_k^{\rm imp}$ expresses the impulsive force accounting for the collisions while the noise term $\boldsymbol{\xi}_k^{(i)}(t) = \xi_{k,\alpha}^{(i)} \boldsymbol{e}_\alpha$ (the unit vector $\boldsymbol{e}_\alpha$ in the α direction) satisfies the fluctuation–dissipation relation [57]:

$$\langle \boldsymbol{\xi}_k^{(i)}(t) \rangle = \boldsymbol{0}, \quad \left\langle \xi_{k,\alpha}^{(i)}(t) \xi_{\ell,\beta}^{(j)}(t') \right\rangle = \frac{2\zeta_i T_{\rm env}}{m_i} \delta_{ij} \delta_{k\ell} \delta_{\alpha\beta} \delta(t - t'). \tag{3}$$

2.2. *Boltzmann equation*

If the density of the solid particles is low enough, the Langevin equation (2) can be converted into the Boltzmann kinetic equation for the distribution function $f_i(\boldsymbol{r}, \boldsymbol{v}, t)$ for the species i of

the dilute binary mixture of inertial suspensions. The set of coupled Boltzmann equations reads

$$\left(\frac{\partial}{\partial t}+\boldsymbol{v}\cdot\nabla\right)f_i(\boldsymbol{r},\boldsymbol{v},t)=\zeta_i\frac{\partial}{\partial\boldsymbol{v}}\cdot\left[\left(\boldsymbol{v}+\frac{T_{\rm env}}{m_i}\frac{\partial}{\partial\boldsymbol{v}}\right)f_i(\boldsymbol{r},\boldsymbol{v},t)\right]+\sum_j J_{ij}\left[\boldsymbol{v}|f_i,f_j\right], \tag{4}$$

with the collision integral [23]

$$J_{ij}\left[\boldsymbol{v}_1|f_i,f_j\right]=\sigma_{12}^{(ij)2}\int d\boldsymbol{v}_2\int d\widehat{\boldsymbol{\sigma}}\Theta\left(\widehat{\sigma}\cdot\boldsymbol{v}_{12}\right)\left(\widehat{\sigma}\cdot\boldsymbol{v}_{12}\right)$$
$$\times\left[\frac{1}{e_{ij}^2}f_i\left(\boldsymbol{r},\boldsymbol{v}_1'',t\right)f_j\left(\boldsymbol{r},\boldsymbol{v}_2'',t\right)-f_i\left(\boldsymbol{r},\boldsymbol{v}_1,t\right)f_j(\boldsymbol{r},\boldsymbol{v}_2,t)\right], \tag{5}$$

where we have introduced $\sigma_{12}^{(ij)}\equiv(\sigma_1^{(i)}+\sigma_2^{(j)})/2$.

From the distribution f_i, one can define the number density of species i as

$$n_i(\boldsymbol{r},t)=\int d\mathbf{v}\ f_i(\boldsymbol{r},\boldsymbol{v},t), \tag{6}$$

the flow velocity $\boldsymbol{U}_i$ of species i as

$$U_i(\boldsymbol{r},t)=\int d\mathbf{v}\ \boldsymbol{v}\ f_i(\boldsymbol{r},\boldsymbol{v},t), \tag{7}$$

and the partial temperature T_i of species i as

$$\frac{3}{2}n_i(\boldsymbol{r},t)T_i(\boldsymbol{r},t)=\int d\mathbf{v}\ \frac{m}{2}V(\boldsymbol{r},t)^2\ f_i(\boldsymbol{r},\boldsymbol{v},t). \tag{8}$$

Here, $\boldsymbol{V}(\boldsymbol{r},t)\equiv\boldsymbol{v}-\boldsymbol{U}(\boldsymbol{r},t)$ is the peculiar velocity. The mean flow velocity $\boldsymbol{U}(\boldsymbol{r},t)$ and the kinetic temperature $T(\boldsymbol{r},t)$ are defined, respectively, as

$$\boldsymbol{U}=\rho^{-1}\sum_i\ \rho_i\boldsymbol{U}_i,\quad T=\sum_i\ \nu_iT_i, \tag{9}$$

where $n\equiv n_1+n_2$ is the total number density, $\rho_i\equiv m_in_i$ is the mass density of species i, $\rho\equiv\rho_1+\rho_2$ is the total mass density, and $\nu_i\equiv n_i/n=N_i/N$ is the fraction of species i. Here, N_i is the number of particles of species i and $N=N_1+N_2$.

Let us consider the macroscopic velocity satisfying

$$\boldsymbol{U}_1=\boldsymbol{U}_2=\boldsymbol{U}=\dot\gamma y\boldsymbol{e}_x, \tag{10}$$

where $\dot\gamma$ is the constant shear rate. In terms of the peculiar velocity $\mathbf{V}$, Eq. (4) can be rewritten as

$$\left[\frac{\partial}{\partial t}+(\boldsymbol{V}+\dot\gamma y\boldsymbol{e}_x)\cdot\nabla-\dot\gamma V_y\frac{\partial}{\partial V_x}\right]f_i(\boldsymbol{r},\boldsymbol{V},t)$$
$$=\zeta_i\frac{\partial}{\partial\boldsymbol{V}}\cdot\left[\left(\boldsymbol{V}+\frac{T_{\rm env}}{m_i}\frac{\partial}{\partial\boldsymbol{V}}\right)f_i(\boldsymbol{r},\boldsymbol{V},t)\right]+\sum_j J_{ij}\left[\boldsymbol{V}|f_i,f_j\right]. \tag{11}$$

At a macroscopic level, the USF is characterized by uniform density and temperature and a linear velocity field (10). In addition, at a more fundamental level, the USF is defined as that which is spatially uniform in the Lagrangian frame moving with the velocity field (10). In this frame, $f_i(\boldsymbol{r},\boldsymbol{v},t)=f_i(\boldsymbol{V},t)$ and Eq. (11) is reduced to the equation for the velocity distribution function:

$$\left(\frac{\partial}{\partial t}-\dot\gamma V_y\frac{\partial}{\partial V_x}\right)f_i(\boldsymbol{V},t)=\zeta_i\frac{\partial}{\partial\boldsymbol{V}}\cdot\left[\left(\boldsymbol{V}+\frac{T_{\rm env}}{m_i}\frac{\partial}{\partial\boldsymbol{V}}\right)f_i(\boldsymbol{V},t)\right]+\sum_j J_{ij}\left[\boldsymbol{V}|f_i,f_j\right]. \tag{12}$$

One of our theoretical goals is to determine the pressure tensor

$$P_{\alpha\beta}=P_{\alpha\beta}^{(1)}+P_{\alpha\beta}^{(2)}, \tag{13}$$

where the partial pressure tensor for species i is defined as

$$P_{\alpha\beta}^{(i)} = \int d\boldsymbol{V} m_i V_\alpha V_\beta f_i(\boldsymbol{V}). \tag{14}$$

We use Greek and Latin characters for $\{x, y, z\}$ and the species $\{1, 2\}$, respectively. The knowledge of the pressure tensor allows one to obtain the rheological properties of the inertial suspension. Needless to say, the flow under USF is independent of the spatial position by its definition. Therefore, we can start from Eq. (12) as the basic equation for the theoretical analysis.

3. Rheology under uniform shear flows

In this section, we present the results of rheology for a binary mixture of inertial suspension under USF obtained from the Boltzmann equation (12). There are three subsections in this section. In the first subsection, we summarize a general framework to determine the rheology of inertial suspensions by deriving a set of equations for the partial pressure tensors by multiplying both sides of Eq. (12) by $m_i \boldsymbol{V}\boldsymbol{V}$ and integrating over velocity. No approximations are considered in this subsection, including the moment of the collision integral (5). In the second subsection, we focus on the steady rheology within the framework of the kinetic theory under Grad's moment method [58]. In the third subsection, we explain the concrete procedure to determine the steady rheology.

3.1. *Moment equation for the pressure tensor*

As mentioned before, the set of equations for the pressure tensor of the species i is obtained by multiplying by $m_i V_\alpha V_\beta$ both sides of the Boltzmann equation (12) and integrating over $\boldsymbol{V}$. The result is

$$\frac{\partial}{\partial t} P_{\alpha\beta}^{(i)} + \dot{\gamma}\left(\delta_{\alpha x} P_{y\beta}^{(i)} + \delta_{\beta x} P_{y\alpha}^{(i)}\right) = -2\zeta_i\left(P_{\alpha\beta}^{(i)} - n_i T_{\rm env}\delta_{\alpha\beta}\right) - \sum_{j=1}^{2} \Lambda_{\alpha\beta}^{(ij)}, \quad i = 1, 2, \tag{15}$$

where $\boldsymbol{\Lambda}^{(ij)}$ is the collisional moment

$$\Lambda_{\alpha\beta}^{(ij)} \equiv -\int d\boldsymbol{V} m_i V_\alpha V_\beta J_{ij}\left[\boldsymbol{V}|f_i, f_j\right]. \tag{16}$$

Let us introduce the anisotropic temperatures

$$\Delta T_i \equiv \frac{P_{xx}^{(i)} - P_{yy}^{(i)}}{n_i}, \quad \Delta T \equiv \frac{P_{xx} - P_{yy}}{n}. \tag{17}$$

It should be noted that there are some other anisotropic temperatures such as $\delta T \equiv (P_{xx} - P_{zz})/n$, which differ from ΔT in general. Nevertheless, we ignore the difference between ΔT and δT in this paper, because (i) the detection of the difference between ΔT and δT is difficult [13] and (ii) the linear approximation of Grad's method used later yields $P_{yy}^{(i)} = P_{zz}^{(i)}$ and so, $\Delta T = \delta T$. In general, δT differs from ΔT even for dilute systems (see Refs. [10,11]), although the previous studies confirmed that the effect of $\delta T \neq \Delta T$ is small [11,13]. We also want to indicate that the difference between ΔT and δT is almost imperceptible in the simulations (see Appendix A) despite the requirement of long and tedious calculations for evaluating this difference [13]. Therefore, for simplicity, we ignore the difference between ΔT and δT in this paper.

If we adopt such a simplification, the evolution equations for T_i, ΔT_i, and $P_{xy}^{(i)}$ are given by

$$\frac{\partial}{\partial t} T_i = -\frac{2}{3n_i}\dot{\gamma} P_{xy}^{(i)} + 2\zeta_i(T_{\rm env} - T_i) - \frac{1}{3n_i}\sum_{j=1}^{2}\Lambda_{\alpha\alpha}^{(ij)}, \tag{18a}$$

$$\frac{\partial}{\partial t}\Delta T_i = -\frac{2}{n_i}\dot{\gamma} P_{xy}^{(i)} - 2\zeta_i \Delta T_i - \frac{1}{n_i}\sum_{j=1}^{2}\left(\Lambda_{xx}^{(ij)} - \Lambda_{yy}^{(ij)}\right), \tag{18b}$$

$$\frac{\partial}{\partial t}P_{xy}^{(i)} = -\dot{\gamma} n_i\left(T_i - \frac{1}{3}\Delta T_i\right) - 2\zeta_i P_{xy}^{(i)} - \sum_{j=1}^{2}\Lambda_{xy}^{(ij)}, \tag{18c}$$

where we have introduced the environmental temperature T_{env} of the suspension liquid. Note that the diagonal elements of the pressure tensor in dilute systems can be written as

$$P_{xx}^{(i)} = n_i\left(T_i + \frac{2}{3}\Delta T_i\right), \tag{19}$$

$$P_{yy}^{(i)} = n_i\left(T_i - \frac{1}{3}\Delta T_i\right). \tag{20}$$

In this paper, we adopt Einstein's rule for the summation, i.e., $P_{\alpha\alpha}^{(i)} = \sum_{\alpha=1}^{3} P_{\alpha\alpha}^{(i)}$. Upon deriving Eq. (19), we recall that we have made use of the identity $P_{yy}^{(i)} = P_{zz}^{(i)}$.

3.2. *Kinetic theory of rheology for a dilute binary mixture of inertial suspension via Grad's method*

3.2.1. *Grad's moment method for the velocity distribution function.* To determine $P_{\alpha\beta}^{(i)}$, we need to know the explicit form of the collisional moments $\Lambda_{\alpha\beta}^{(ij)}$. This requires knowledge of the velocity distribution functions f_i, which is an intricate problem even for the elastic case. As for monodisperse inertial suspensions, a useful way to estimate $\boldsymbol{\Lambda}^{(ij)}$ is to adopt Grad's moment method [58] in which the true f_i is approximated by the trial Grad's distribution [11,12,15,16,26,58–60]:

$$f_i(\boldsymbol{V}) \approx f_{i,\text{M}}(\boldsymbol{V})\left(1 + \frac{m_i}{2T_i}\Pi_{\alpha\beta}^{(i)} V_\alpha V_\beta\right), \tag{21}$$

where

$$\Pi_{\alpha\beta}^{(i)} = \frac{P_{\alpha\beta}^{(i)}}{n_i T_i} - \delta_{\alpha\beta}, \tag{22}$$

and $f_{i,\text{M}}(\boldsymbol{V})$ is the Maxwellian distribution at the temperature T_i of the species i, i.e.,

$$f_{i,\text{M}}(\boldsymbol{V}) = n_i\left(\frac{m_i}{2\pi T_i}\right)^{3/2}\exp\left(-\frac{m_i V^2}{2T_i}\right). \tag{23}$$

Note that in Eq. (21) we have taken into account that the mass and heat fluxes of a binary mixture vanish in the USF state.

With the use of the distribution (21), the integrals appearing in the expression of the collisional moments $\boldsymbol{\Lambda}^{(ij)}$ can be explicitly computed. After a lengthy calculation (see Appendix B for the derivation), one gets

$$\Lambda_{\alpha\beta}^{(ij)} = \frac{2\sqrt{\pi}}{3} n_i n_j m_{ij}\sigma_{12}^{(ij)2} v_{\text{T}}^3\left(\frac{\epsilon_i + \epsilon_j}{\epsilon_i\epsilon_j}\right)^{3/2}(1+e_{ij})\left\{\left[\lambda_{ij} - \frac{1}{2}\frac{m_{ij}}{m_i}(1+e_{ij})\right]\delta_{\alpha\beta}\right.$$
$$\left. + 2\frac{\epsilon_i\epsilon_j}{(\epsilon_i+\epsilon_j)^2}\left[\left(1 + \frac{3}{5}\frac{\epsilon_i+\epsilon_j}{\epsilon_i}\lambda_{ij}\right)\Pi_{\alpha\beta}^{(i)} - \left(1 - \frac{3}{5}\frac{\epsilon_i+\epsilon_j}{\epsilon_j}\lambda_{ij}\right)\Pi_{\alpha\beta}^{(j)}\right]\right\}, \tag{24}$$

with

$$\lambda_{ij} \equiv 2\frac{m_i\epsilon_j - m_j\epsilon_i}{(m_i+m_j)(\epsilon_i+\epsilon_j)} + \frac{1}{2}\frac{m_{ij}}{m_i}(3 - e_{ij}). \tag{25}$$

Here, we have introduced $\epsilon_i \equiv m_i T/(\overline{m} T_i)$, and the thermal velocity $v_{\rm T} \equiv \sqrt{2T/\overline{m}}$ with the mean mass $\overline{m}$ defined as $\overline{m} \equiv (m_1 + m_2)/2$. Upon deriving Eq. (24), nonlinear terms in the traceless stress tensor $\Pi_{\alpha\beta}^{(i)}$ have been neglected (linear Grad's approximation). The expression (24) agrees with a previous derivation of the collision integral $\Lambda_{\alpha\beta}^{(ij)}$ [47].

Now, let us rewrite the set of Eqs. (18) in dimensionless forms. We introduce the partial dimensionless temperatures θ_i and the anisotropic temperatures $\Delta\theta_i$ for species i as

$$\theta_i \equiv \frac{T_i}{T_{\rm env}}, \quad \Delta\theta_i \equiv \frac{\Delta T_i}{T_{\rm env}}. \tag{26}$$

We also introduce the global quantities $\theta \equiv \sum_{i=1}^2 \nu_i \theta_i$ and $\Delta\theta \equiv \sum_{i=1}^2 \nu_i \Delta\theta_i$, where we recall that $\nu_i = n_i/n$.

Then, the dimensionless collisional moment

$$\Lambda_{\alpha\beta}^{(ij)*} \equiv \frac{\Lambda_{\alpha\beta}^{(ij)}}{n_i \overline{\sigma}^{-1} \sqrt{T_{\rm env}^3/\overline{m}}} \tag{27}$$

becomes

$$\Lambda_{\alpha\beta}^{(ij)*} = C_{ij}\theta^{3/2} \left(\frac{\epsilon_i + \epsilon_j}{\epsilon_i \epsilon_j}\right)^{3/2} \left\{ \left[\lambda_{ij} - \frac{1}{2}\frac{m_{ij}}{m_i}(1 + e_{ij}) \right] \delta_{\alpha\beta} + 2\frac{\epsilon_i \epsilon_j}{(\epsilon_i + \epsilon_j)^2} \left[\left(1 + \frac{3}{5}\frac{\epsilon_i + \epsilon_j}{\epsilon_i}\lambda_{ij}\right) \Pi_{\alpha\beta}^{(i)} - \left(1 - \frac{3}{5}\frac{\epsilon_i + \epsilon_j}{\epsilon_j}\lambda_{ij}\right) \Pi_{\alpha\beta}^{(j)} \right] \right\}, \tag{28}$$

with

$$C_{ij} \equiv 8\sqrt{\frac{2}{\pi}} \frac{\nu_j}{\nu_1 \sigma^{(1)*3} + \nu_2 \sigma^{(2)*3}} m_{ij}^* \sigma^{(ij)*2} \varphi (1 + e_{ij}), \tag{29}$$

where we have introduced the packing fraction

$$\varphi \equiv \frac{\pi}{6} n (\nu_1 \sigma^{(1)3} + \nu_2 \sigma^{(2)3}). \tag{30}$$

In addition, the dimensionless reduced mass $m_{ij}^* \equiv m_i^* m_j^*/(m_i^* + m_j^*)$, $m_i^* \equiv m_i/\overline{m}$, $\sigma^{(i)*} \equiv \sigma_i/\overline{\sigma}$, $\sigma^{(ij)*} \equiv \sigma^{(ij)}/\overline{\sigma}$, and

$$\xi_{\rm env} \equiv \sqrt{\frac{T_{\rm env}}{\overline{m}}} \frac{1}{\overline{\sigma}\overline{\zeta}} \tag{31}$$

characterizes the magnitude of the noise [13]. In terms of the temperature ratio

$$\vartheta \equiv \frac{T_1}{T_2}, \tag{32}$$

the partial temperatures T_1 and T_2 can be written as

$$\frac{T_1}{T} = \frac{\vartheta}{\nu_2 + \nu_1 \vartheta}, \quad \frac{T_2}{T} = \frac{1}{\nu_2 + \nu_1 \vartheta}, \tag{33}$$

$$\theta_1 = \frac{T_1}{T}\frac{T}{T_{\rm env}} = \frac{\vartheta\theta}{\nu_2 + \nu_1 \vartheta}, \quad \theta_2 = \frac{\theta}{\nu_2 + \nu_1 \vartheta}. \tag{34}$$

Therefore, the parameters ϵ_i ($i = 1, 2$) can be expressed as

$$\epsilon_1 = \frac{m_i}{\overline{m}}\frac{\theta}{\theta_1} = \frac{m_1}{\overline{m}}\frac{\nu_2 + \nu_1\vartheta}{\vartheta}, \quad \epsilon_2 = \frac{m_2}{\overline{m}}(\nu_2 + \nu_1 \vartheta). \tag{35}$$

Using these variables, we rewrite the set of Eqs. (18) as

$$\frac{\partial}{\partial\tau}\theta_i = -\frac{2}{3}\dot{\gamma}^*\theta_i \Pi_{xy}^{(i)} + 2\zeta_i^*(1 - \theta_i) - \frac{1}{3}\sum_{j=1}^2 \Lambda_{\alpha\alpha}^{(ij)*}, \tag{36a}$$

$$\frac{\partial}{\partial\tau}\Delta\theta_i = -2\dot{\gamma}^*\theta_i\Pi_{xy}^{(i)} - 2\zeta_i^*\Delta\theta_i - \sum_{j=1}^{2}\left(\Lambda_{xx}^{(ij)*} - \Lambda_{yy}^{(ij)*}\right), \tag{36b}$$

$$\frac{\partial}{\partial\tau}\left(\theta_i\Pi_{xy}^{(i)}\right) = -\dot{\gamma}^*\left(\theta_i - \frac{1}{3}\Delta\theta_i\right) - 2\zeta_i^*\theta_i\Pi_{xy}^{(i)} - \sum_{j=1}^{2}\Lambda_{xy}^{(ij)*}, \tag{36c}$$

where we have introduced the scaled time $\tau \equiv t\sqrt{T_{\rm env}/\overline{m}}/\overline{\sigma}$, the dimensionless shear rate $\dot{\gamma}^* \equiv \dot{\gamma}\overline{\sigma}\sqrt{\overline{m}/T_{\rm env}} = \dot{\gamma}/(\overline{\zeta}\xi_{\rm env})$, and the dimensionless drag coefficient $\zeta_i^* \equiv \zeta_i\overline{\sigma}\sqrt{\overline{m}/T_{\rm env}} = \zeta_i/(\overline{\zeta}\xi_{\rm env})$. For the sake of convenience, some explicit forms of $\Lambda_{\alpha\beta}^{(ij)*}$ in Eq. (24) can be rewritten as

$$\Lambda_{\alpha\alpha}^{(ij)*} = 3C_{ij}\theta^{3/2}\widetilde{\Lambda}_{\alpha\alpha}^{(ij)}, \tag{37a}$$

$$\Lambda_{xx}^{(ij)*} - \Lambda_{yy}^{(ij)*} = 2C_{ij}\theta^{3/2}\left[\widetilde{\Lambda}_{xy}^{(ij)}\Delta\theta_i - \widetilde{\Lambda}_{xy}^{\prime(ij)}\Delta\theta_j\right], \tag{37b}$$

$$\Lambda_{xy}^{(ij)*} = 2C_{ij}\theta^{3/2}\left[\widetilde{\Lambda}_{xy}^{(ij)}\theta_i\Pi_{xy}^{(i)} - \widetilde{\Lambda}_{xy}^{\prime(ij)}\theta_j\Pi_{xy}^{(j)}\right], \tag{37c}$$

where

$$\widetilde{\Lambda}_{\alpha\alpha}^{(ij)} \equiv \left(\frac{\epsilon_i+\epsilon_j}{\epsilon_i\epsilon_j}\right)^{3/2}\left[2\frac{m_i^*\epsilon_j - m_j^*\epsilon_i}{(m_i^*+m_j^*)(\epsilon_i+\epsilon_j)} + \frac{m_{ij}^*}{m_i^*}(1-e_{ij})\right], \tag{38a}$$

$$\widetilde{\Lambda}_{xy}^{(ij)} \equiv \frac{\theta_i^{-1}}{\sqrt{\epsilon_i\epsilon_j(\epsilon_i+\epsilon_j)}}\left(1 + \frac{3}{5}\frac{\epsilon_i+\epsilon_j}{\epsilon_i}\lambda_{ij}\right), \tag{38b}$$

$$\widetilde{\Lambda}_{xy}^{\prime(ij)} \equiv \frac{\theta_j^{-1}}{\sqrt{\epsilon_i\epsilon_j(\epsilon_i+\epsilon_j)}}\left(1 - \frac{3}{5}\frac{\epsilon_i+\epsilon_j}{\epsilon_j}\lambda_{ij}\right). \tag{38c}$$

3.3. *Theoretical expressions in the steady rheology*

Although the set of Eqs. (36) applies for time-dependent states, we are mainly interested in the rheology in the steady state. Hereafter, we focus on the steady rheology.

3.3.1. *Theoretical flow curves in the steady state.*

Let us solve the set of Eqs. (36) in the steady state. In this case ($\partial_\tau = 0$), the left-hand side of the set (36) vanishes and one gets

$$0 = -\frac{2}{3}\dot{\gamma}^*\theta_i\Pi_{xy}^{(i)} + 2\zeta_i^*(1-\theta_i) - \sum_{j=1}^{2}C_{ij}\widetilde{\Lambda}_{\alpha\alpha}^{(ij)}\theta^{3/2}, \tag{39a}$$

$$0 = -2\dot{\gamma}^*\theta_i\Pi_{xy}^{(i)} - 2\zeta_i^*\Delta\theta_i - 2\sum_{j=1}^{2}C_{ij}\theta^{3/2}\left[\widetilde{\Lambda}_{xy}^{(ij)}\Delta\theta_i - \widetilde{\Lambda}_{xy}^{\prime(ij)}\Delta\theta_j\right], \tag{39b}$$

$$0 = -\dot{\gamma}^*\left(\theta_i - \frac{1}{3}\Delta\theta_i\right) - 2\zeta_i^*\theta_i\Pi_{xy}^{(i)} - 2\sum_{j=1}^{2}C_{ij}\theta^{3/2}\left[\widetilde{\Lambda}_{xy}^{(ij)}\theta_i\Pi_{xy}^{(i)} - \widetilde{\Lambda}_{xy}^{\prime(ij)}\theta_j\Pi_{xy}^{(j)}\right]. \tag{39c}$$

First, from Eq. (39a), one obtains

$$\Pi_{xy}^{(i)} = \frac{3}{\dot{\gamma}^*\theta_i}\left[\zeta_i^*(1-\theta_i) - \frac{1}{2}\sum_{j=1}^{2}C_{ij}\widetilde{\Lambda}_{\alpha\alpha}^{(ij)}\theta^{3/2}\right]. \tag{40}$$

Substituting Eq. (40) into Eq. (39b), the set of equations that determine $\Delta\theta_1$ and $\Delta\theta_2$ can be rewritten as

$$F_{i1}\Delta\theta_1 + F_{i2}\Delta\theta_2 = G_i, \tag{41}$$

for $i = 1, 2$. Here, we have introduced the quantities

$$F_{11}(\theta, \vartheta) \equiv \zeta_1^* + \left[C_{11}\left(\widetilde{\Lambda}_{xy}^{(11)} - \widetilde{\Lambda}_{xy}^{\prime(11)}\right) + C_{12}\widetilde{\Lambda}_{xy}^{(12)}\right]\theta^{3/2}, \quad F_{12}(\theta, \vartheta) \equiv -C_{12}\widetilde{\Lambda}_{xy}^{\prime(12)}\theta^{3/2}, \tag{42a}$$

$$F_{22}(\theta, \vartheta) \equiv \zeta_2^* + \left[C_{22}\left(\widetilde{\Lambda}_{xy}^{(22)} - \widetilde{\Lambda}_{xy}^{\prime(22)}\right) + C_{21}\widetilde{\Lambda}_{xy}^{(21)}\right]\theta^{3/2}, \quad F_{21}(\theta, \vartheta) \equiv -C_{21}\widetilde{\Lambda}_{xy}^{\prime(21)}\theta^{3/2}, \tag{42b}$$

and

$$G_1(\theta, \vartheta) \equiv -3\zeta_1^*(1-\theta_1) + \frac{3}{2}\left[C_{11}\widetilde{\Lambda}_{\alpha\alpha}^{(11)} + C_{12}\widetilde{\Lambda}_{\alpha\alpha}^{(12)}\right]\theta^{3/2}, \tag{43a}$$

$$G_2(\theta, \vartheta) \equiv -3\zeta_2^*(1-\theta_2) + \frac{3}{2}\left[C_{21}\widetilde{\Lambda}_{\alpha\alpha}^{(21)} + C_{22}\widetilde{\Lambda}_{\alpha\alpha}^{(22)}\right]\theta^{3/2}. \tag{43b}$$

Then, $\Delta\theta_1$ and $\Delta\theta_2$ can be expressed as

$$\Delta\theta_1(\theta, \vartheta) = \frac{G_1F_{22} - G_2F_{12}}{F_{11}F_{22} - F_{12}F_{21}}, \quad \Delta\theta_2(\theta, \vartheta) = \frac{G_2F_{11} - G_1F_{21}}{F_{11}F_{22} - F_{12}F_{21}}. \tag{44}$$

Substituting Eqs. (40) and (44) into Eq. (39c) leads to the relationship

$$H_1(\theta, \vartheta)K_2(\theta, \vartheta) = H_2(\theta, \vartheta)K_1(\theta, \vartheta), \tag{45}$$

where

$$H_1(\theta, \vartheta) \equiv -2\left(F_{11}\dot{\gamma}^*\theta_1\Pi_{xy}^{(1)} + F_{12}\dot{\gamma}^*\theta_2\Pi_{xy}^{(2)}\right), \tag{46a}$$

$$H_2(\theta, \vartheta) \equiv -2\left(F_{21}\dot{\gamma}^*\theta_1\Pi_{xy}^{(1)} + F_{22}\dot{\gamma}^*\theta_2\Pi_{xy}^{(2)}\right), \tag{46b}$$

and

$$K_1(\theta, \vartheta) \equiv \theta_1 - \frac{1}{3}\Delta\theta_1, \quad K_2(\theta, \vartheta) \equiv \theta_2 - \frac{1}{3}\Delta\theta_2. \tag{47}$$

Equation (45) determines the relationship between the (reduced) global kinetic temperature θ and the temperature ratio ϑ. For given values of the mixture and at a given value of θ, we determine the temperature ratio ϑ [defined in Eq. (32)] by numerically solving Eq. (45). As will be shown in the next section, we find a solution of θ by fixing ϑ in the intermediate-shear regime where the size ratio becomes large by fixing the volume ratio. Once we determine this relationship, we can draw the flow curve with the aid of Eq. (45), where the shear rate is given by

$$\dot{\gamma}^* = \sqrt{\frac{H_1(\theta, \vartheta)}{K_1(\theta, \vartheta)}}. \tag{48}$$

4. Comparison between theory and simulation

In this section, we compare the theoretical results obtained in Sect. 3 with those of EDL-SHS [18]. We will consider binary mixtures constituted by species of the same mass density [$m_1/m_2 = (\sigma^{(1)}/\sigma^{(2)})^3$] and a (common) coefficient of restitution [$e_{11} = e_{12} = e_{21} = e_{22} \equiv e$]. In the first subsection, we examine the case of an equimolar mixture ($\nu_1 = \nu_2 = 1/2$ or $N_1 = N_2$) while the general case of $N_1 \neq N_2$ will be analyzed in the second subsection. In particular, we find a new DST-like rheological phase transition for $N_1 \ll N_2$ when we fix the volume ratio, i.e., a binary mixture in which the concentration of one of the species (the large tracer particles 1) is much smaller than that of the other species (the small particles 2).

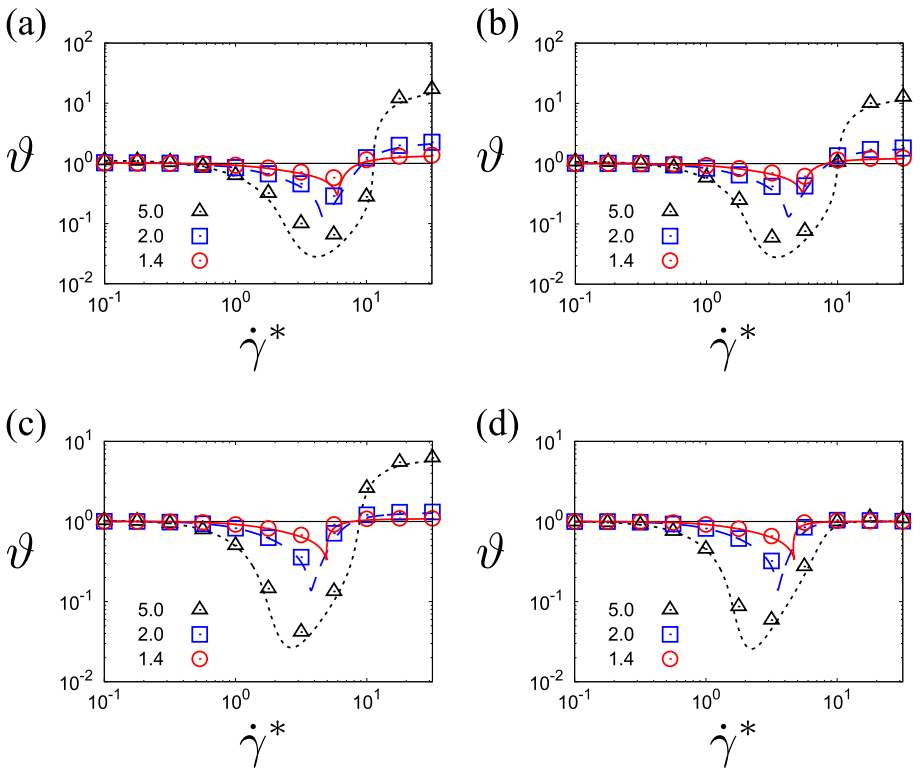

Fig. 2. Temperature ratio $\vartheta = T_1/T_2$ against the dimensionless shear rate $\dot{\gamma}^*$ for $\sigma^{(1)}/\sigma^{(2)} = 1.4$ (solid line and open circles), 2.0 (dashed line and open squares), and 5.0 (dotted line and open triangles) when we fix $\varphi = 0.01$, $\xi_{\rm env} = 1.0$, and $\nu_1 = \nu_2 = 1/2$ for (a) $e = 0.5$, (b) 0.7, (c) 0.9, and (d) 1. The lines and symbols correspond to the steady theoretical solutions (48) and the simulation results ($N = 1000$), respectively.

4.1. *The rheology for $N_1 = N_2$*

In this subsection, we present the results of EDLSHS to verify the validity of the predictions of the kinetic theory for $N_1 = N_2$. In this case, we should note that the occupied volume is dominated by large grains for a large size ratio $\sigma^{(1)}/\sigma^{(2)}$. For example, the ratio of occupied volumes $\mathcal{V} \equiv N_1\sigma^{(1)3}/(N_2\sigma^{(2)3})$ becomes 125 if we adopt $\sigma^{(1)}/\sigma^{(2)} = 5.0$. The results of EDLSHS under the control of N_1/N_2 with fixed $\mathcal{V}$ will be discussed in the next subsection. For the comparison of the theoretical results with those of EDLSHS, we have used the steady solutions of Eqs. (39) for both the elastic ($e = 1$) and inelastic ($e = 0.5$, 0.7, and 0.9) cases when we fix $N = 1000$, $\varphi = 0.01$, $\xi_{\rm env} = 1.0$, and $\nu_1 = \nu_2 = 1/2$.

Figures 2 (for $\vartheta = T_1/T_2$) and 3 (for η_1/η_2) show some characteristic rheological flow curves for binary mixtures for both elastic and inelastic cases. Here, we have introduced the viscosity η_i for species i as

$$\eta_i \equiv -P_{xy}^{(i)}/\dot{\gamma}. \tag{49}$$

Now, let us focus on the plot of the temperature ratio $\vartheta \equiv T_1/T_2$ against the reduced shear rate $\dot{\gamma}^*$ in Fig. 2. In the low-shear regime, the temperature ratio converges to unity as shown in Fig. 2. This is because the temperatures of both the larger and smaller particles are determined by the thermal noise of the background fluid. On the other hand, the temperature ratio converges to a constant in the high-shear regime, which is determined by the interparticle inelastic collisions. Note that this converged value agrees with the one previously obtained for granular gases [47].

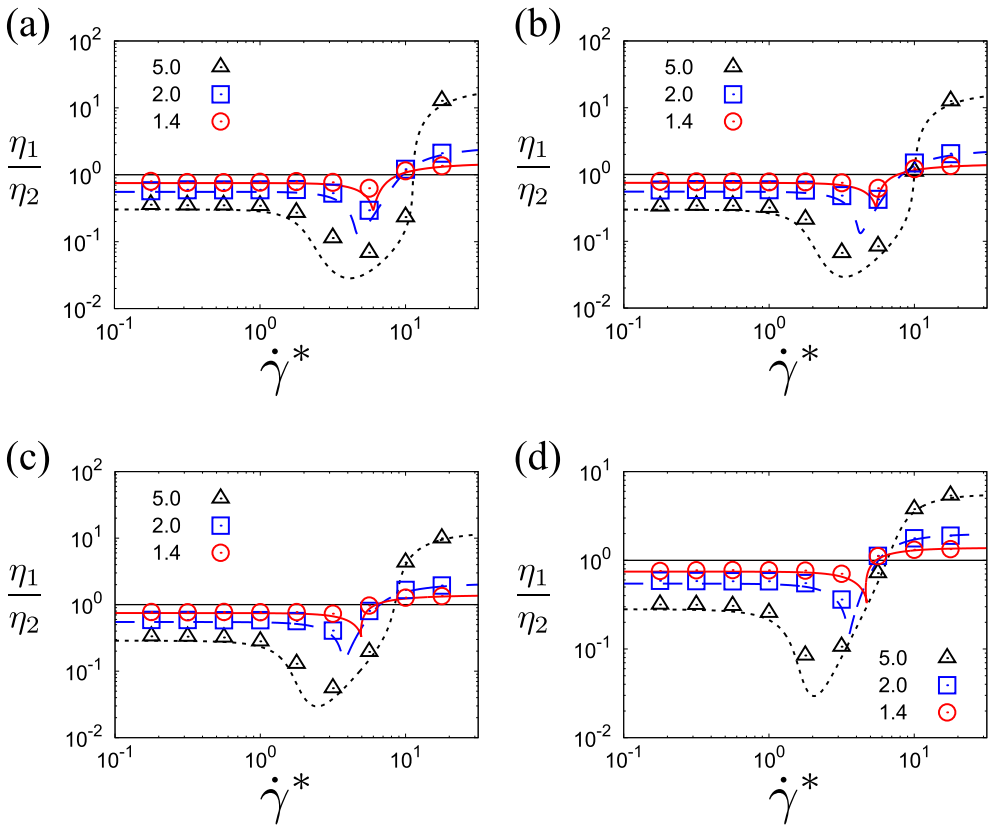

Fig. 3. Viscosity ratio η_1/η_2 against the dimensionless shear rate $\dot{\gamma}^*$ for $\sigma^{(1)}/\sigma^{(2)} = 1.4$ (solid line and open circles), 2.0 (dashed line and open squares), and 5.0 (dotted line and open triangles) when we fix $\varphi = 0.01$, $\xi_{\rm env} = 1.0$, and $\nu_1 = \nu_2 = 1/2$ for (a) $e = 0.5$, (b) 0.7, (c) 0.9, and (d) 1. The lines and symbols correspond to the steady theoretical solutions (49) and the simulation results ($N = 1000$), respectively.

Interestingly, our theory predicts the existence of a negative peak for ϑ in the intermediate-shear regime. In particular, there exists a cusp for smaller values of $\sigma^{(1)}/\sigma^{(2)}$ at a certain shear rate $\dot{\gamma}_{\rm c}^*$ (at which $|\partial\vartheta/\partial\dot{\gamma}^*| \to \infty$; see Fig. 2). Correspondingly, the ratios of the other quantities such as η_1/η_2 exhibit cusps around $\dot{\gamma}_{\rm c}^*$ (see Fig. 3). It is worth remarking that these observables exhibit common features since (i) they do not have sharp minima even near the DST-like transition point of one of two species, (ii) the deviations from unity become larger with increasing size ratio $\sigma^{(1)}/\sigma^{(2)}$, and (iii) the ratios converge to values different from unity even in the low-shear limit. These singularities are inherently connected with the DST-like transition observed (see Appendix C) for the global kinetic temperature θ and the shear viscosity $\eta^* = \eta_1^* + \eta_2^*$ [$\eta_i^* \equiv \eta_i/(nT_{\rm env}/\overline{\zeta})$ with Eq. (49)] because the cusps vanish as the size ratio increases. Indeed, the flow curves for ϑ and η_1/η_2 become smooth for $\sigma^{(1)}/\sigma^{(2)} = 5.0$ (see Figs. 2 and 3).

Let us also discuss the existence of cusps in the flow curves observed in Figs. 2 and 3 when the size ratio is small. As shown in Fig. 4, the partial viscosities η_i^* also have discontinuous jumps when the mean viscosity $\eta^* = \eta_1^* + \eta_2^*$ also has this jump. At points ($\dot{\gamma}_{\rm c}$) where $\partial\eta_i^*/\partial\dot{\gamma}^* \to \pm\infty$ ($i = 1, 2$) are satisfied, the viscosity ratio also diverges as

$$\frac{\partial}{\partial\dot{\gamma}^*}\left(\frac{\eta_1^*}{\eta_2^*}\right) = \frac{1}{\eta_2^{*2}}\left(\frac{\partial\eta_1^*}{\partial\dot{\gamma}^*}\eta_2^* - \eta_1^*\frac{\partial\eta_2^*}{\partial\dot{\gamma}^*}\right) \to \pm\infty. \tag{50}$$

This is the reason for the existence of the cusps.

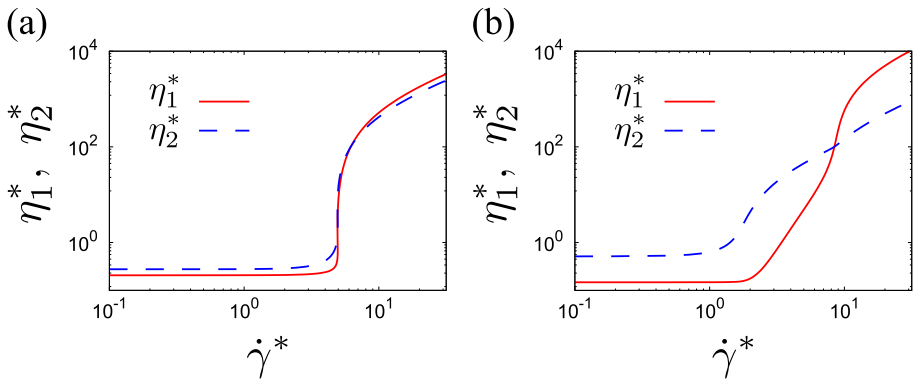

Fig. 4. Plots of the dimensionless partial viscosities η_1^* and η_2^* against the dimensionless shear rate $\dot{\gamma}^*$ for (a) $\sigma^{(1)}/\sigma^{(2)} = 1.4$ and (b) 5.0 when we fix $\varphi = 0.01$, $\xi_{\rm env} = 1.0$, and $\nu_1 = \nu_2 = 1/2$.

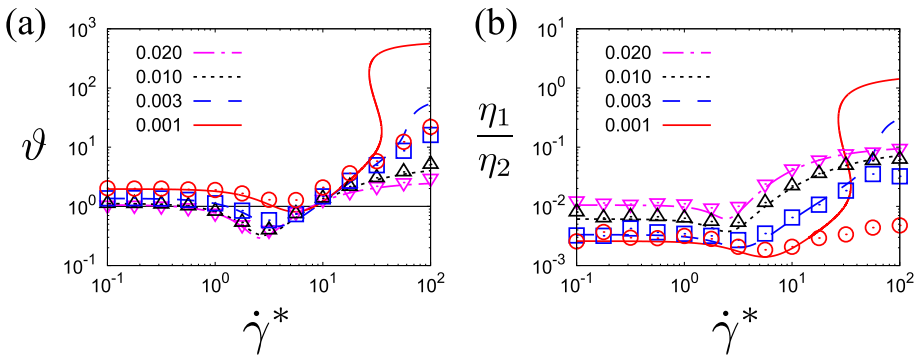

Fig. 5. (a) Temperature ratio ϑ against the dimensionless shear rate $\dot{\gamma}^*$ for $\nu_1 = 1.0 \times 10^{-3}$ (solid line and open circles), 3.0×10^{-3} (dashed line and open squares), 1.0×10^{-2} (dotted line and open upper triangles), and 2.0×10^{-2} (dot–dashed line and open lower triangles) when we fix $\varphi = 0.01$, $\xi_{\rm env} = 1.0$, $e = 0.9$, and $\mathcal{V} = 1$. (b) Viscosity ratio η_1/η_2 against the dimensionless shear rate $\dot{\gamma}$ for the same set of parameters. All results of simulations are obtained for $N = 1000$.

It is remarkable that the predictions of kinetic theory agree well with the simulation results of EDLSHS without any fitting parameter. Therefore, we conclude that our kinetic theory based on the Boltzmann equation with Grad's method is reliable to describe the rheology, at least for $N_1 = N_2$.

To close this subsection, we also note that the flow curves become discontinuous and continuous depending on the other parameters of the mixture. These behaviors are discussed in Appendix D.

4.2. *The rheology for $N_1 \neq N_2$*

In this subsection, we compare the simulation results for the rheology for $N_1 \neq N_2$ with those derived from the theoretical predictions by fixing the volume ratio $\mathcal{V} \equiv N_1\sigma^{(1)3}/(N_2\sigma^{(2)3}) = 1$. This means that the volume occupied by the large particles is the same as that by the small ones. From the definition of the volume ratio, the size ratio correspondingly becomes $\sigma^{(1)}/\sigma^{(2)} = (N_2/N_1)^{1/3} = [(1-\nu_1)/\nu_1]^{1/3}$. Thus, as the size ratio increases, the number of collisions between large particles decreases. On the other hand, the impulse from the larger particle at each collision increases as compared with that from the smaller particle.

Figures 5(a) and (b) plot the results of ϑ and η_1/η_2, respectively, against $\dot{\gamma}^*$ for $\nu_1 = 1.0 \times 10^{-3}$

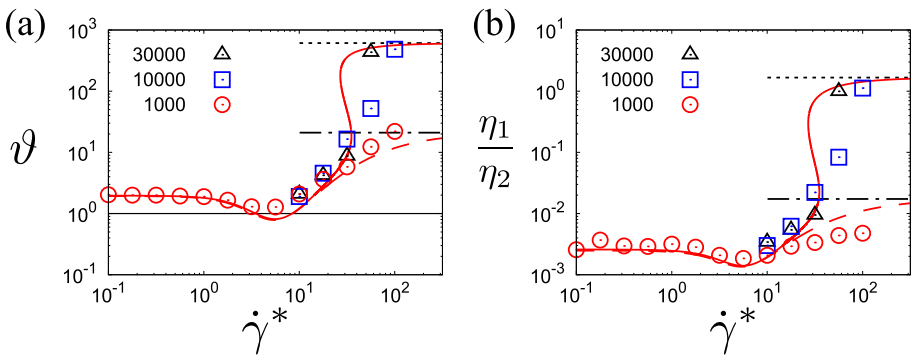

Fig. 6. (a) Temperature ratio ϑ and (b) viscosity ratio η_1/η_2 against the dimensionless shear rate $\dot{\gamma}^*$ for $N = 1000$ (open circles), 10 000 (open squares), and 30 000 (open triangles) when we fix $\varphi = 0.01$, $\xi_{\rm env} = 1.0$, $e = 0.9$, $\mathcal{V} = 1$, and $\nu_1 = 1.0 \times 10^{-3}$. The solid and dashed lines indicate the theoretical curves for Eqs. (48) and (49) and the tracer limit explained in Appendix E, respectively. The dotted and dot–dashed lines represent the granular gas limits for Eqs. (48) and (49) and that under the tracer limit in Appendix E, respectively.

(solid line and open circles), 3.0×10^{-3} (dashed line and open squares), 1.0×10^{-2} (dotted line and open upper triangles), and 2.0×10^{-2} (dot–dashed line and open lower triangles) by fixing $\varphi = 0.01$, $e = 0.9$, and $\xi_{\rm env} = 1.0$. Here, the corresponding size ratios become (a) $\sigma^{(1)}/\sigma^{(2)} = 10.0$, (b) 6.93, (c) 4.63, and (d) 3.66, respectively. It should be noted that the number of particles of EDLSHS is fixed as $N = 1000$ in Fig. 5. It is quite apparent that the theory compares well with the simulation results in a wide range of shear rates and without any fitting parameters when the size ratio is not large (or equivalently, $\nu_1 \gtrsim 3.0 \times 10^{-3}$ in Fig. 5). On the other hand, some discrepancies between the theoretical prediction and the EDLSHS simulations are observed in the high-shear regime when the size ratio becomes sufficiently large (see the data for $\nu_1 = 1.0 \times 10^{-3}$ in Fig. 5). In particular, at $\dot{\gamma}^* \approx 30$, the theory predicts a new DST-like transition in which the flow curve becomes S-shaped; in this region the temperature ratio versus the shear rate becomes a multivalued function [see Fig. 5(a)]. Here, the upper branch becomes almost 100 times larger compared to the lower branch. This behavior is analogous to the ignited–quenched transitions for the shear-rate dependence of both the temperature and the viscosity for the monodisperse case [13,15]. (See Appendix D for the minimum value of the size ratio at which this transition occurs.) The origin of the discrepancy between theory and simulations is essentially associated with the suppression of the collisions between the large (tracer) particles because the number of them becomes $N_1 \sim \mathcal{O}(1)$ for $\sigma^{(1)}/\sigma^{(2)} \gg 1$, as discussed in the following.

To verify our conjecture, we examine the simulation results obtained for different large system sizes: $N = 10\,000$ and 30 000. We find that the disagreement between theory and simulation tends to decrease as the number of particles in the EDLSHS increases. As an illustration, Fig. 6 shows the dependence of both the temperature ratio ϑ and the viscosity ratio η_1/η_2 on the number of particles N when we fix $\nu_1 = 1.0 \times 10^{-3}$. Here, the relationships between the total number of particles and that of large particles correspond to $(N, N_1) = (1000, 1)$, (10 000, 10), and (30 000, 30). As N_1 increases, the effect of collisions between large particles on rheology becomes non-negligible. The collisions between large particles affect the flow curve in particular in the high-shear regime. Correspondingly, the quantities discontinuously change at a certain shear rate; this shear rate depends on the number of particles. The above results suggest that (i) the discontinuous change predicted by the kinetic theory can be universally observed in the

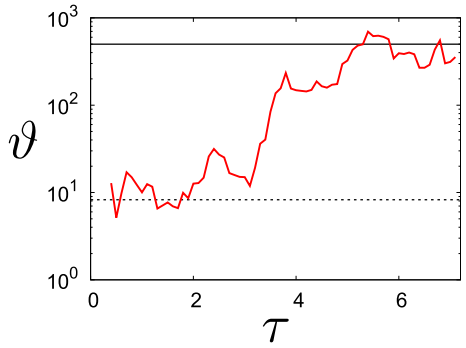

Fig. 7. Time evolution of the temperature ratio ϑ when we fix $\varphi = 0.01$, $\xi_{\rm env} = 1.0$, $e = 0.9$, $N = 30\,000$, $\mathcal{V} = 1$, $\dot{\gamma}^* = 5.6 \times 10^2$, and $\nu_1 = 1.0 \times 10^{-3}$, where we have introduced the dimensionless time $\tau \equiv t\sqrt{T_{\rm env}/\overline{m}}/\overline{\sigma}$. The solid line refers to the solution obtained for a binary mixture assisted by Eqs. (45) and (48) with $\nu_1 = 1.0 \times 10^{-3}$ while the dashed line corresponds to the analytical result obtained in Appendix E in the tracer limit.

thermodynamic limit and (ii) the picture of an impurity enslaved to the host fluid (namely, when the tracer–tracer collisions are neglected) is insufficient to capture the above discontinuous transition. The fact that the seemingly natural "enslaved impurity" picture breaks down for large shear rates has been shown to also be responsible for the extreme violation of energy equipartition in a sheared granular mixture in the tracer limit [61,62].

We can also understand this finite-size effect of EDLSHS when we observe the time evolution of the temperature ratio ϑ for a very large system. Figure 7 exhibits the typical evolution of ϑ for $N = 30\,000$. The solid line refers to the solution obtained for a binary mixture assisted by Eq. (45) with $\nu_1 = 1.0 \times 10^{-3}$ while the dashed line corresponds to the analytical result obtained in Appendix E in the tracer limit (i.e., by neglecting collisions between tracer particles and by assuming that the excess species 2 is not affected by the presence of tracer particles). We observe transient behavior in the result of EDLSHS from the tracer limit line (dashed line) to that of the (complete) solution including collisions between large particles (solid line). It is apparent that collisions between large tracer particles do not play any role in the early stage since the temperature ratio measured in the simulation agrees well with the tracer limit line (see the data for $\tau \lesssim 2$ in Fig. 7). As time goes on, however, those contributions become important for the rheology of the system. As a result, the temperature ratio measured in EDLSHS starts to increase abruptly (see the data for $\tau \simeq 3$ in Fig. 7), and tends to converge to the asymptotic theoretical value ($\tau \gtrsim 5$).

Let us check how the discontinuous changes of the temperature ratio and the viscosity ratio appear in the thermodynamic limit. According to Fig. 5, there must exist a critical value $\nu_{1,\rm c}$ of the fraction in the range $1.0 \times 10^{-3} < \nu_{1,\rm c} < 3.0 \times 10^{-3}$. The discontinuity is characterized by a point (i) at which $\partial\vartheta/\partial\dot{\gamma}^* \to \infty$ in the higher temperature regime and where (ii) the curve of ϑ versus $\dot{\gamma}^*$ discontinuously changes in the lower regime. Here, we introduce a critical temperature ratio $\vartheta_{\rm c}$, which satisfies the identities

$$\left(\frac{\partial\dot{\gamma}^*}{\partial\vartheta}\right)_{e,\varphi,\nu_1} = 0, \quad \left(\frac{\partial^2\dot{\gamma}^*}{\partial\vartheta^2}\right)_{e,\varphi,\nu_1} = 0. \tag{51}$$

The relations (51) are analogous to the critical point at the first-order transition [15]. Figure 8 shows the dependence of both the phase coexistence line ($\partial\dot{\gamma}^*/\partial\vartheta = 0$) and the spinodal line

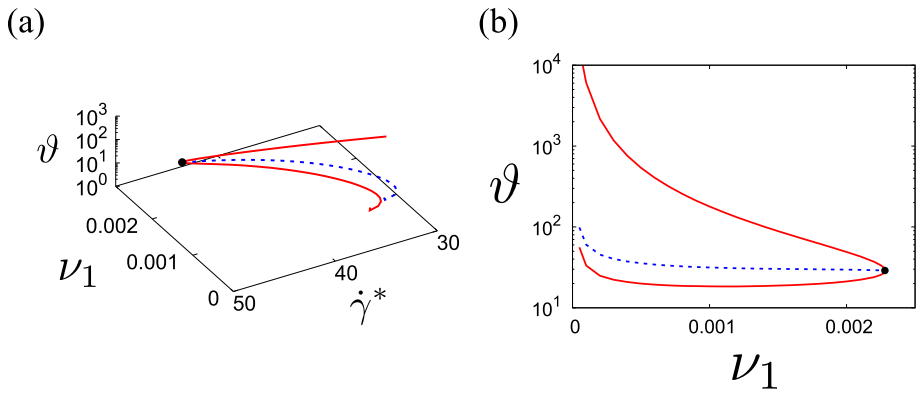

Fig. 8. (a) Plot of the phase coexistence line $\partial\dot{\gamma}^*/\partial\vartheta = 0$ (solid lines) and the spinodal line $\partial^2\dot{\gamma}^*/\partial\vartheta^2 = 0$ (dashed line) for $\varphi = 0.01$, $\xi_{\rm env} = 1.0$, $e = 0.9$, and $\mathcal{V} = 1$. (b) Plot of the projection of the phase coexistence line and the spinodal line onto the (ν_1, ϑ) plane. The point indicates the critical point $(\nu_1, \dot{\gamma}^*, \vartheta) \simeq (2.28 \times 10^{-2}, 45.9, 28.9)$.

$(\partial^2\dot{\gamma}^*/\partial\vartheta^2 = 0)$ on the fraction fraction ν_1 for $\varphi = 0.01$, $\xi_{\rm env} = 1.0$, $e = 0.9$, and $\mathcal{V} = 1$. As expected, these lines converge to the critical values $\nu_1 \simeq 2.28 \times 10^{-2}$, $\dot{\gamma}^* \simeq 45.9$, and $\vartheta \simeq 28.9$. The finding of a DST-like rheological phase transition in the large shear-rate region if the size ratio is large on fixing the volume ratio is one of the most interesting results achieved in this paper.

4.3. *Velocity distribution function*

In this subsection, let us compare the velocity distribution function (VDF) (21) of Grad's moment method with the one obtained by means of simulations. As a complement, we also include the exact VDF of a BGK-like kinetic model in the large shear limit (see Appendix F).

For later analysis, let us introduce the dimensionless velocity $\boldsymbol{c}$ and the distribution function $g_{i,\rm G}(\boldsymbol{c})$ as

$$\boldsymbol{c} \equiv \sqrt{\frac{m_i}{2T_i}}\boldsymbol{V}, \quad g_{i,\rm G}(\boldsymbol{c}) \equiv \left(\frac{2T_i}{m_i}\right)^{3/2}\frac{f_{i,\rm G}(\boldsymbol{V})}{n_i}, \tag{52}$$

where $f_{i,\rm G}$ stands for Grad's VDF (21) for species i. Now, we focus on the VDF of the larger particles 1. It is convenient to consider the marginal distribution $g_{1,\rm G}^{(xy)}$ instead of using the full 3D VDF. The distribution $g_{1,\rm G}^{(xy)}$ is defined as

$$\begin{aligned} g_{1,\rm G}^{(xy)}(c_x, c_y) &= \int_{-\infty}^{\infty} dc_z g_{1,\rm G}(\boldsymbol{c}) \\ &= g_{1,\rm M}^{(xy)}(c_x, c_y)\left[1 + \left(\frac{1}{2} + c_y^2 - 2c_x^2\right)\Pi_{yy}^{(1)} + 2c_x c_y \Pi_{xy}^{(1)}\right], \end{aligned} \tag{53}$$

where

$$g_{1,\rm M}^{(xy)}(c_x, c_y) = \frac{1}{\pi}e^{-(c_x^2+c_y^2)}. \tag{54}$$

The VDF $g_{1,\rm G}^{(x,y)}(c_x, c_y)$ in Eq. (53) can characterize the anisotropy of the VDF induced by the shear flow.

Figures 9 and 10 present $g_{1,\rm G}^{(xy)}(c_x, c_y) - g_{1,\rm M}^{(xy)}(c_x, c_y)$ for $\dot{\gamma}^* = 0.32$, 1.0, 3.2, 10, and 32. These values of the shear rate belong to the lower (0.32 and 1.0), intermediate (3.2 and 10), and higher

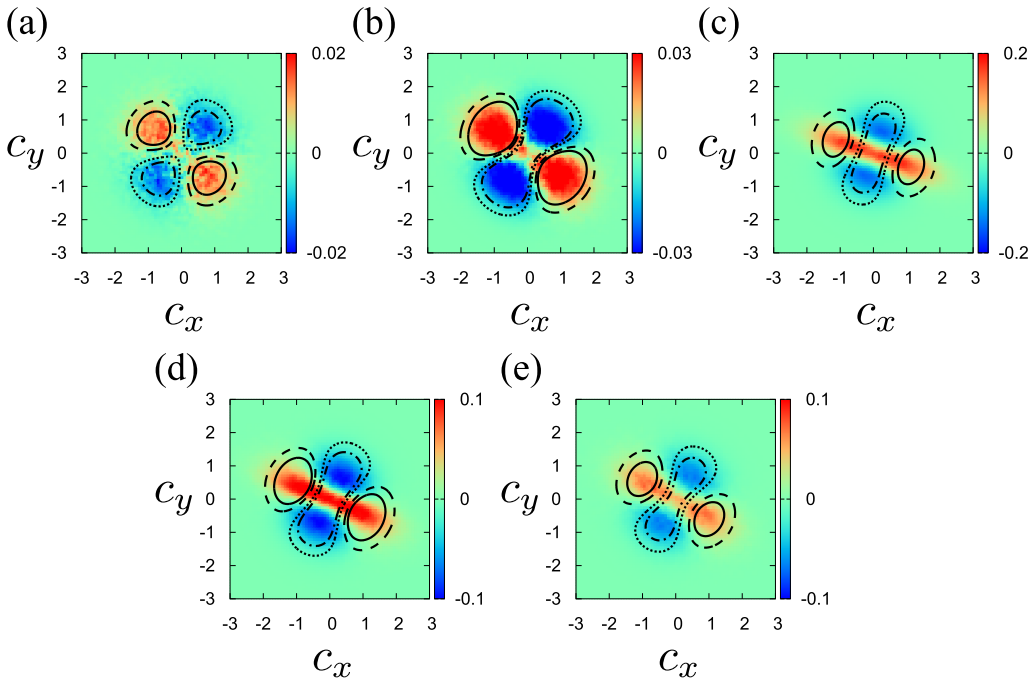

Fig. 9. Velocity distribution functions of the larger particles $g_{1,\mathrm{G}}^{(xy)}(c_x, c_y) - g_{1,\mathrm{M}}^{(xy)}(c_x, c_y)$ in the (c_x, c_y) plane for (a) $\dot{\gamma}^* = 0.32$, (b) 1.0, (c) 3.2, (d) 10, and (e) 32 when we fix $\varphi = 0.01$, $e = 0.9$, $\xi_{\mathrm{env}} = 1.0$, $\sigma^{(1)}/\sigma^{(2)} = 2.0$, and $\nu_1 = \nu_2 = 1/2$. The color plot corresponds to the simulation results. The solid, dashed, dotted, and dot–dashed lines represent the contours $0.2c_{\max}$, $0.1c_{\max}$, $-0.1c_{\max}$, and $-0.2c_{\max}$ obtained from Grad's method (53) with (a) $c_{\max} = 0.02$, (b) 0.03, (c) 0.2, and (d, e) 0.1, respectively.

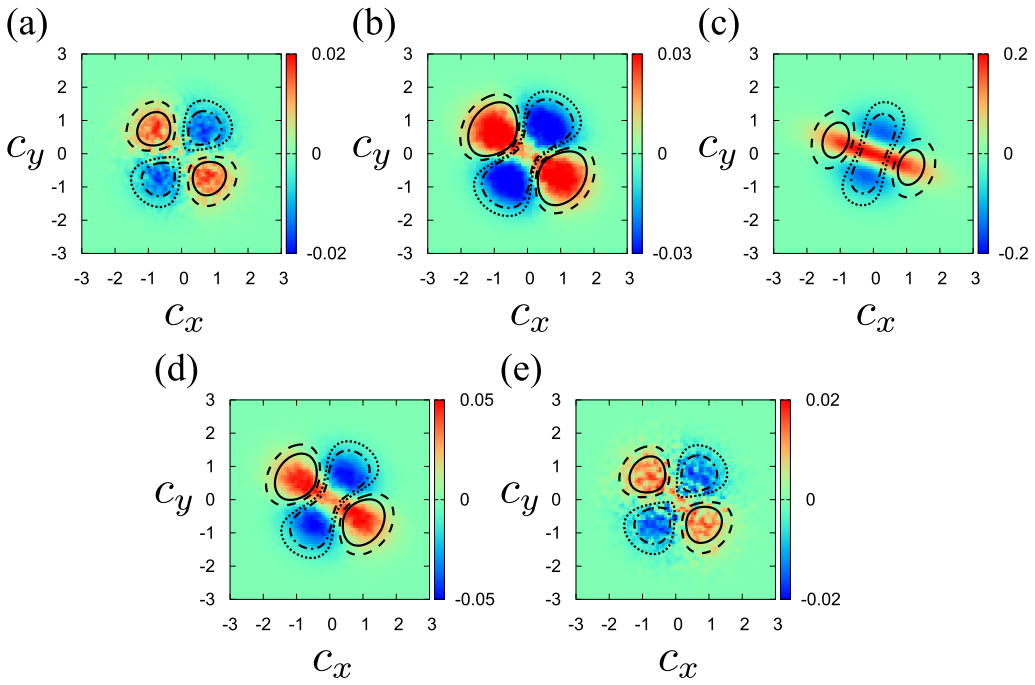

Fig. 10. Velocity distribution functions of the larger particles $g_{1,\mathrm{G}}^{(xy)}(c_x, c_y) - g_{1,\mathrm{M}}^{(xy)}(c_x, c_y)$ in the (c_x, c_y) plane for (a) $\dot{\gamma}^* = 0.32$, (b) 1.0, (c) 3.2, (d) 10, and (e) 32 when we fix $\varphi = 0.01$, $e = 1.0$, $\xi_{\mathrm{env}} = 1.0$, $\sigma^{(1)}/\sigma^{(2)} = 2.0$, and $\nu_1 = \nu_2 = 1/2$. The color plot corresponds to the simulation results. The solid, dashed, dotted, and dot–dashed lines represent the contours $0.2c_{\max}$, $0.1c_{\max}$, $-0.1c_{\max}$, and $-0.2c_{\max}$ obtained from Grad's method (53) with (a) $c_{\max} = 0.02$, (b) 0.03, (c) 0.2, (d) 0.05, and (e) 0.02, respectively.

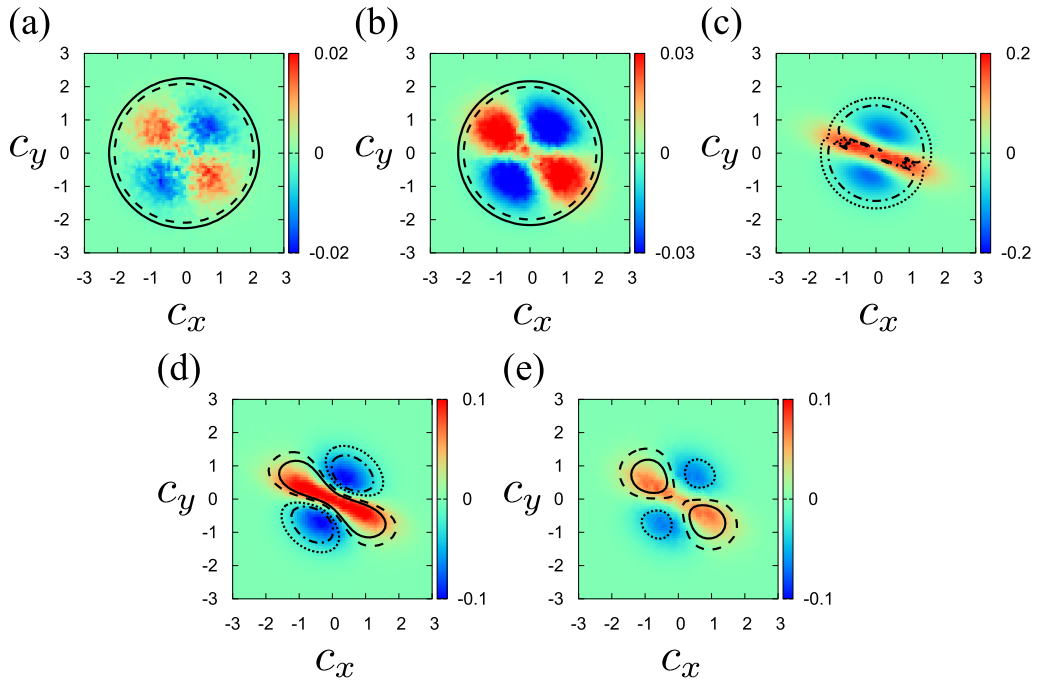

Fig. 11. Velocity distribution functions of the larger particles $g_{1,\mathrm{G}}^{(xy)}(c_x, c_y) - g_{1,\mathrm{M}}^{(xy)}(c_x, c_y)$ in the (c_x, c_y) plane for (a) $\dot{\gamma}^* = 0.32$, (b) 1.0, (c) 3.2, (d) 10, and (e) 32 when we fix $\varphi = 0.01$, $e = 0.9$, $\xi_{\mathrm{env}} = 1.0$, $\sigma^{(1)}/\sigma^{(2)} = 2.0$, and $\nu_1 = \nu_2 = 1/2$. The color plot corresponds to the simulation results. The solid, dashed, dotted, and dot–dashed lines represent the contours $0.2c_{\max}$, $0.1c_{\max}$, $-0.1c_{\max}$, and $-0.2c_{\max}$ obtained from the BGK model (F16) with (a) $c_{\max} = 0.02$, (b) 0.03, (c) 0.2, and (d, e) 0.1, respectively.

(32) branches of the flow curve for $e = 0.9$ in Fig. 9 and $e = 1$ in Fig. 10, respectively. It is remarkable that Grad's distribution works well in the wide range of the shear rate as shown in Figs. 9 and 10. The corresponding trends are clearly observed when we consider the 1D VDF in the x direction (see Appendix G). Nevertheless, it seems that the enhancement of the VDF in the shear direction is underestimated in the theoretical prediction. It should be noted that this enhancement is suppressed for the 1D VDF, as shown in Appendix G.

We also check whether the VDF obtained from the BGK-like model can be used (see Appendix F for details). As expected, the deviation of the distribution of the BGK-like model from that of the simulation is large for the low-shear regime. On the other hand, the agreement between BGK and simulations is reasonable in the high-shear regime (see Fig. 11). In particular, the BGK distribution is more accurate than Grad's in the small-velocity region. In any case, it is important to recall that the BGK distribution obtained in Appendix F only holds when $T_{\mathrm{env}} = 0$. This means that the possible discrepancies between the BGK distribution and simulations can be in part due to the fact that $T_{\mathrm{env}} \neq 0$ in the simulations.

5. Discussion and conclusion

In this paper, we have theoretically derived the rheology of a dilute binary mixture of inertial suspensions under USF. As in previous papers [15,16], two different but complementary approaches have been employed to solve the set of coupled Boltzmann kinetic equations. On the analytical side, Grad's moment method [58] has been used to approximately solve the Boltzmann equation. Since the mass and heat fluxes vanish in the USF, only the partial traceless stress tensors $\Pi_{\alpha\beta}^{(i)}$ are retained in the trial distribution functions $f_i(\boldsymbol{V})$. Then, the theoretical

predictions for the temperature ratio T_1/T_2 and the viscosity ratio η_1/η_2 were compared against computer simulations based on the event-driven Langevin simulation method. We have confirmed that the theoretical predictions agree with the results of simulation for hard spheres for various size ratios in most parameter regions. We have found that the temperature ratio and viscosity ratio discontinuously change at a certain shear rate as the size ratio increases. This feature cannot be captured by simulations when the size of the system is small. The above transition is similar to DST in dense suspensions or the first-order phase transition at equilibrium. Although the tracer limit of the theory is validated when the system size is small, the collisions between large tracer particles play dominant roles in the high-shear regime. We have also compared the velocity distribution functions obtained by Grad's method and the BGK-like model with those obtained from the simulations.

There are several future perspectives. First, we plan to analyze the mass transport of impurities in a sheared inertial suspension. As already done in Ref. [27], a Chapman–Enskog-like expansion around the local shear flow distribution obtained here will be considered to identify the shear-rate-dependent diffusion $D_{\alpha\beta}$, pressure diffusion $D_{p,\alpha\beta}$, and thermal diffusion $D_{T,\alpha\beta}$ tensors. The determination of $D_{\alpha\beta}$, $D_{p,\alpha\beta}$, and $D_{T,\alpha\beta}$ will be discussed in a forthcoming paper. More importantly, knowledge of the above diffusion tensors will allow us to analyze segregation by thermal diffusion [50]. In the present paper, we have restricted ourselves to homogeneous systems, which makes the analysis easier than that for inhomogeneous systems. However, depending on the size or density of particles, the segregation is inevitable when one considers binary mixtures. In a sheared system, segregation has been observed if there exists an inhomogeneous velocity profile [42]. However, the velocity profile remains linear in our simulations as far as we have checked. This linearity is violated if we consider systems under gravity or wall-driven sheared systems. We believe that this scenario of segregation can be described by a dilute system described by the Boltzmann equation. We will analyze such systems in the near future.

Needless to say, we also plan to extend our analysis to moderately dense systems with the aid of the Enskog equation. The extension is tough but straightforward using a similar procedure to that followed for monodisperse systems [16]. This study will also be carried out in the future.

Acknowledgements

S.T. and H.H. thank K. Saitoh and M. Otsuki for fruitful discussions. The research of S.T. and H.H. was partially supported by a Grant-in-Aid from MEXT for Scientific Research (Grant No. JP21H01006). The research of S.T. and H.H. was also partially supported by Grants-in-Aid from MEXT for Scientific Research (Grant Nos. JP20K14428 and JP16H04025, respectively) and ISHIZUE 2020 of the Kyoto University Research Development Program. The research of V.G. has been supported by the Spanish Government through Grant No. PID2020-112936GB-I00 funded by MCIN/AEI/10.13039/501100011033, from Grant IB20079 funded by Junta de Extremadura (Spain), and by ERDF: A way of making Europe. This work was initiated during a short stay of V.G. at the Yukawa Institute for Theoretical Physics (YITP, Kyoto University) supported by the YITP activity (YITP–T–18–03). V.G. appreciates the warm hospitality of the YITP at that time. S.T. and H.H. also acknowledge the warm hospitality of the Universidad de Extremadura during their stay there in 2020.

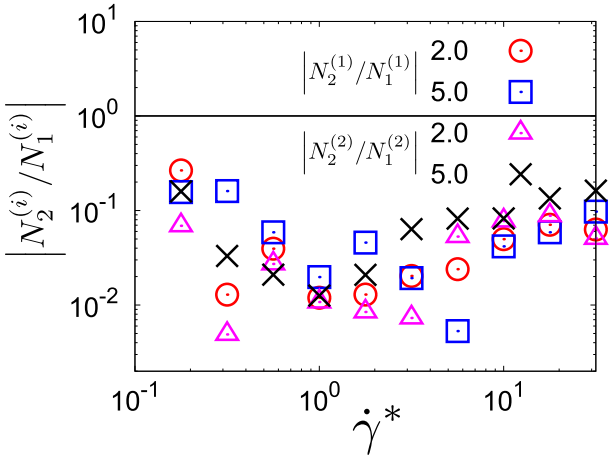

Fig. A1. Plots of the ratio of the second to the first difference of each species i, $|N_2^{(i)}/N_1^{(i)}|$ for $\sigma^{(1)}/\sigma^{(2)} = 2.0$ and 5.0 when we fix $\varphi = 0.01$, $\xi_{\text{env}} = 1.0$, $e = 0.9$, and $\nu_1 = \nu_2 = 1/2$.

Appendix A. Difference between $P_{yy}^{(i)}$ and $P_{zz}^{(i)}$

In this appendix, we show the difference between $P_{yy}^{(i)}$ and $P_{zz}^{(i)}$. As mentioned in the main text, the second normal stress difference of species i, $N_2^{(i)} \equiv P_{yy}^{(i)} - P_{zz}^{(i)}$ is, in general, nonzero. However, the second difference $N_2^{(i)}$ is treated as zero in the dilute limit of the kinetic theory. Figure A1 shows the plot of the ratio of the second to the first normal stress differences against the shear rate for $\sigma^{(1)}/\sigma^{(2)} = 2.0$ and 5.0 obtained from the simulations when we fix $\varphi = 0.01$, $\xi_{\text{env}} = 1.0$, $e = 0.9$, and $\nu_1 = \nu_2 = 1/2$. Here, we have introduced the first normal stress difference of species i as $N_1^{(i)} \equiv P_{xx}^{(i)} - P_{yy}^{(i)}$. However, the second difference $N_2^{(i)}$ has values much smaller than the values of $N_1^{(i)}$ in the wide range of shear rates considered. Therefore, we do not consider the difference between them in this paper. It is noted that the second normal stress difference cannot be neglected when the volume fraction is finite.

Appendix B. Derivation of $\Lambda_{\alpha\beta}^{(ij)}$ under the linear approximation of Grad's expansion

In this appendix, we obtain the expression (24) for the collisional moment $\Lambda_{\alpha\beta}^{(ij)}$. For this purpose, we introduce the dimensionless velocities

$$\begin{cases} \boldsymbol{G} = \dfrac{m_i \boldsymbol{V}_1 + m_j \boldsymbol{V}_2}{(m_i + m_j) v_{\text{T}}}, \\ \boldsymbol{g} = \dfrac{\boldsymbol{V}_1 - \boldsymbol{V}_2}{v_{\text{T}}}, \end{cases} \tag{B1}$$

and equivalently

$$\begin{cases} \boldsymbol{V}_1 = \left(\boldsymbol{G} + \dfrac{m_{ij}}{m_i} \boldsymbol{g} \right) v_{\text{T}}, \\ \boldsymbol{V}_2 = \left(\boldsymbol{G} - \dfrac{m_{ij}}{m_j} \boldsymbol{g} \right) v_{\text{T}}. \end{cases} \tag{B2}$$

Let us rewrite $f_i(\boldsymbol{V}_1) f_j(\boldsymbol{V}_2)$ in terms of $\boldsymbol{G}$ and $\boldsymbol{g}$. Using Grad's trial distribution (21), we can rewrite $f_i(\boldsymbol{V}_1) f_j(\boldsymbol{V}_2)$ as

$$\begin{aligned} & f_i(\boldsymbol{V}_1) f_j(\boldsymbol{V}_2) \\ & = n_i n_j \left(\frac{\overline{m}}{2\pi T}\right)^3 (\epsilon_i \epsilon_j)^{3/2} \\ & \quad \times \exp\left[-(\epsilon_i+\epsilon_j)G^2 - 2\left(\frac{m_{ij}}{m_i}\epsilon_i - \frac{m_{ij}}{m_j}\epsilon_j\right)(\boldsymbol{G}\cdot\boldsymbol{g}) - \left(\frac{m_{ij}^2}{m_i^2}\epsilon_i + \frac{m_{ij}^2}{m_j^2}\epsilon_j\right) g^2\right] \\ & \quad \times \left[1 + \epsilon_i \Pi_{\alpha\beta}^{(i)} \left(G_\alpha + \frac{m_{ij}}{m_i} g_\alpha\right)\left(G_\beta + \frac{m_{ij}}{m_i} g_\beta\right) + \epsilon_j \Pi_{\alpha\beta}^{(j)} \left(G_\alpha - \frac{m_{ij}}{m_j} g_\alpha\right)\left(G_\beta - \frac{m_{ij}}{m_j} g_\beta\right)\right]. \end{aligned} \tag{B3}$$

We note that nonlinear contributions of the stress tensor $\Pi_{\alpha\beta}^{(i)}$ are ignored in this appendix. Let us rewrite the argument of the exponential part in Eq. (B3) as

$$\begin{aligned} & (\epsilon_i+\epsilon_j)G^2 + 2\left(\frac{m_{ij}}{m_i}\epsilon_i - \frac{m_{ij}}{m_j}\epsilon_j\right)(\boldsymbol{G}\cdot\boldsymbol{g}) + \left(\frac{m_{ij}^2}{m_i^2}\epsilon_i + \frac{m_{ij}^2}{m_j^2}\epsilon_j\right) g^2 \\ & = (\epsilon_i+\epsilon_j)\left[\boldsymbol{G} + \frac{m_j\epsilon_i - m_i\epsilon_j}{(m_i+m_j)(\epsilon_i+\epsilon_j)}\boldsymbol{g}\right]^2 + \frac{\epsilon_i\epsilon_j}{\epsilon_i+\epsilon_j} g^2. \end{aligned} \tag{B4}$$

Introducing $\boldsymbol{G}'$ as

$$\boldsymbol{G}' \equiv \boldsymbol{G} + \frac{m_j\epsilon_i - m_i\epsilon_j}{(m_i+m_j)(\epsilon_i+\epsilon_j)}\boldsymbol{g}, \tag{B5}$$

one gets the identities

$$\begin{cases} \boldsymbol{G} + \dfrac{m_{ij}}{m_i}\boldsymbol{g} = \boldsymbol{G}' + \dfrac{\epsilon_j}{\epsilon_i+\epsilon_j}\boldsymbol{g}, \\ \boldsymbol{G} - \dfrac{m_{ij}}{m_j}\boldsymbol{g} = \boldsymbol{G}' - \dfrac{\epsilon_i}{\epsilon_i+\epsilon_j}\boldsymbol{g}. \end{cases} \tag{B6}$$

Thus, we can rewrite Eq. (B3) as

$$\begin{aligned} f_i(\boldsymbol{V}_1) f_j(\boldsymbol{V}_2) = n_i n_j v_{\mathrm{T}}^{-3} (\epsilon_i\epsilon_j)^{3/2} \pi^{-3} \exp\left[-(\epsilon_i+\epsilon_j)G'^2 - \frac{\epsilon_i\epsilon_j}{\epsilon_i+\epsilon_j} g^2\right] \\ \times \left[1 + \epsilon_i \Pi_{\alpha\beta}^{(i)} \left(G'_\alpha + \frac{\epsilon_j}{\epsilon_i+\epsilon_j} g_\alpha\right)\left(G'_\beta + \frac{\epsilon_j}{\epsilon_i+\epsilon_j} g_\beta\right)\right. \\ \left. + \epsilon_j \Pi_{\alpha\beta}^{(j)} \left(G'_\alpha - \frac{\epsilon_i}{\epsilon_i+\epsilon_j} g_\alpha\right)\left(G'_\beta - \frac{\epsilon_i}{\epsilon_i+\epsilon_j} g_\beta\right)\right]. \end{aligned} \tag{B7}$$

Let us rewrite Eq. (16). From Eqs. (1) and (B5), one gets

$$\begin{aligned} m_i v'_{1,\alpha} v'_{1,\beta} - m_i v_{1,\alpha} v_{1,\beta} &= -m_{ij}(1+e_{ij}) v_{\mathrm{T}}^2 (\boldsymbol{g}\cdot\widehat{\boldsymbol{\sigma}}) \\ &\quad \times \left[\left(G_\alpha + \frac{m_{ij}}{m_i} g_\alpha\right)\widehat{\sigma}_\beta + \left(G_\beta + \frac{m_{ij}}{m_i} g_\beta\right)\widehat{\sigma}_\alpha - \frac{m_{ij}}{m_i}(1+e_{ij})(\boldsymbol{g}\cdot\widehat{\boldsymbol{\sigma}})\widehat{\sigma}_\alpha\widehat{\sigma}_\beta\right] \\ &= -m_{ij}(1+e_{ij}) v_{\mathrm{T}}^2 (\boldsymbol{g}\cdot\widehat{\boldsymbol{\sigma}}) \\ &\quad \times \left[G'_\alpha\widehat{\sigma}_\beta + G'_\beta\widehat{\sigma}_\alpha + \frac{\epsilon_j}{\epsilon_i+\epsilon_j}(g_\alpha\widehat{\sigma}_\beta + g_\beta\widehat{\sigma}_\alpha) - \frac{m_{ij}}{m_i}(1+e_{ij})(\boldsymbol{g}\cdot\widehat{\boldsymbol{\sigma}})\widehat{\sigma}_\alpha\widehat{\sigma}_\beta\right]. \end{aligned} \tag{B8}$$

Using Eqs. (B3) and (B8), we can rewrite the collisional moment $\Lambda_{\alpha\beta}^{(ij)}$ as

$$\Lambda_{\alpha\beta}^{(ij)} = m_{ij}(1+e_{ij})n_i n_j \sigma^{(ij)2}(\epsilon_i\epsilon_j)^{3/2} v_{\rm T}^3 \widetilde{\Lambda}_{\alpha\beta}^{(ij)}, \tag{B9}$$

with the linear collisional moment

$$\begin{aligned}
\widetilde{\Lambda}_{\alpha\beta}^{(ij)} \equiv \pi^{-3} \int d\boldsymbol{G}' \int d\boldsymbol{g} \int d\widehat{\boldsymbol{\sigma}} \Theta(\widehat{\boldsymbol{\sigma}}\cdot\boldsymbol{g})(\widehat{\boldsymbol{\sigma}}\cdot\boldsymbol{g})^2 \exp\left[-(\epsilon_i+\epsilon_j)G'^2 - \frac{\epsilon_i\epsilon_j}{\epsilon_i+\epsilon_j}g^2\right] \\
\times \left[G'_\alpha\widehat{\sigma}_\beta + G'_\beta\widehat{\sigma}_\alpha + \frac{\epsilon_j}{\epsilon_i+\epsilon_j}(g_\alpha\widehat{\sigma}_\beta + g_\beta\widehat{\sigma}_\alpha) - \frac{m_{ij}}{m_i}(1+e_{ij})(\boldsymbol{g}\cdot\widehat{\boldsymbol{\sigma}})\widehat{\sigma}_\alpha\widehat{\sigma}_\beta\right] \\
\times \left[1 + \epsilon_i\Pi_{\gamma\delta}^{(i)}\left(G'_\gamma + \frac{\epsilon_j}{\epsilon_i+\epsilon_j}g_\gamma\right)\left(G'_\delta + \frac{\epsilon_j}{\epsilon_i+\epsilon_j}g_\delta\right)\right. \\
\left. + \epsilon_j\Pi_{\gamma\delta}^{(j)}\left(G'_\gamma - \frac{\epsilon_i}{\epsilon_i+\epsilon_j}g_\gamma\right)\left(G'_\delta - \frac{\epsilon_i}{\epsilon_i+\epsilon_j}g_\delta\right)\right].
\end{aligned} \tag{B10}$$

For further calculation, let us first introduce $\widetilde{I}_{ij}^{(\ell)}(\widehat{\boldsymbol{\sigma}})$ and $\widetilde{I}_{ij,\alpha}^{(\ell)}(\widehat{\boldsymbol{\sigma}})$ as

$$\begin{aligned}
\begin{Bmatrix} \widetilde{I}_{ij}^{(\ell)}(\widehat{\boldsymbol{\sigma}}) \\ \widetilde{I}_{ij,\alpha}^{(\ell)}(\widehat{\boldsymbol{\sigma}}) \end{Bmatrix} &\equiv \frac{1}{\pi^3}\int d\boldsymbol{G}' \int d\boldsymbol{g}\Theta(\widehat{\boldsymbol{\sigma}}\cdot\boldsymbol{g})(\widehat{\boldsymbol{\sigma}}\cdot\boldsymbol{g})^\ell \begin{Bmatrix} 1 \\ g_\alpha \end{Bmatrix} \exp\left[-(\epsilon_i+\epsilon_j)G'^2 - \frac{\epsilon_i\epsilon_j}{\epsilon_i+\epsilon_j}g^2\right] \\
&\times \left[1 + \epsilon_i\Pi_{\gamma\delta}^{(i)}\left(G'_\gamma + \frac{\epsilon_j}{\epsilon_i+\epsilon_j}g_\gamma\right)\left(G'_\delta + \frac{\epsilon_j}{\epsilon_i+\epsilon_j}g_\delta\right)\right. \\
&\left. + \epsilon_j\Pi_{\gamma\delta}^{(j)}\left(G'_\gamma - \frac{\epsilon_i}{\epsilon_i+\epsilon_j}g_\gamma\right)\left(G'_\delta - \frac{\epsilon_i}{\epsilon_i+\epsilon_j}g_\delta\right)\right] \\
&= \frac{1}{\pi^{3/2}(\epsilon_i+\epsilon_j)^{3/2}}\int d\boldsymbol{g}\Theta(\widehat{\boldsymbol{\sigma}}\cdot\boldsymbol{g})(\widehat{\boldsymbol{\sigma}}\cdot\boldsymbol{g})^\ell \begin{Bmatrix} 1 \\ g_\alpha \end{Bmatrix} \exp\left(-\frac{\epsilon_i\epsilon_j}{\epsilon_i+\epsilon_j}g^2\right)\mathcal{P}_1(\{g\}),
\end{aligned} \tag{B11}$$

with

$$\mathcal{P}_1(\{g\}) \equiv 1 + \frac{\epsilon_i\epsilon_j^2}{(\epsilon_i+\epsilon_j)^2}g_\gamma g_\delta\Pi_{\gamma\delta}^{(i)} + \frac{\epsilon_i^2\epsilon_j}{(\epsilon_i+\epsilon_j)^2}g_\gamma g_\delta\Pi_{\gamma\delta}^{(j)}. \tag{B12}$$

We also introduce $\widehat{I}_{ij,\alpha}^{(\ell)}(\widehat{\boldsymbol{\sigma}})$ as

$$\begin{aligned}
\widehat{I}_{ij,\alpha}^{(\ell)}(\widehat{\boldsymbol{\sigma}}) &\equiv \frac{1}{\pi^3}\int d\boldsymbol{G}' \int d\boldsymbol{g}\Theta(\widehat{\boldsymbol{\sigma}}\cdot\boldsymbol{g})(\widehat{\boldsymbol{\sigma}}\cdot\boldsymbol{g})^\ell G'_\alpha \exp\left[-(\epsilon_i+\epsilon_j)G'^2 - \frac{\epsilon_i\epsilon_j}{\epsilon_i+\epsilon_j}g^2\right] \\
&\times \left[1 + \epsilon_i\Pi_{\gamma\delta}^{(i)}\left(G'_\gamma + \frac{\epsilon_j}{\epsilon_i+\epsilon_j}g_\gamma\right)\left(G'_\delta + \frac{\epsilon_j}{\epsilon_i+\epsilon_j}g_\delta\right)\right. \\
&\left. + \epsilon_j\Pi_{\gamma\delta}^{(j)}\left(G'_\gamma - \frac{\epsilon_i}{\epsilon_i+\epsilon_j}g_\gamma\right)\left(G'_\delta - \frac{\epsilon_i}{\epsilon_i+\epsilon_j}g_\delta\right)\right] \\
&= \frac{1}{\pi^{3/2}(\epsilon_i+\epsilon_j)^{3/2}}\int d\boldsymbol{g}\Theta(\widehat{\boldsymbol{\sigma}}\cdot\boldsymbol{g})(\widehat{\boldsymbol{\sigma}}\cdot\boldsymbol{g})^\ell \exp\left(-\frac{\epsilon_i\epsilon_j}{\epsilon_i+\epsilon_j}g^2\right)\mathcal{Q}_{1,\alpha}(\{g\}),
\end{aligned} \tag{B13}$$

with

$$\mathcal{Q}_{1,\alpha}(\{g\}) = \frac{\epsilon_i\epsilon_j}{(\epsilon_i+\epsilon_j)^2}g_\gamma\left(\Pi_{\alpha\gamma}^{(i)} - \Pi_{\alpha\gamma}^{(j)}\right). \tag{B14}$$

Using Eqs. (B11) and (B13), Eq. (B10) is rewritten as

$$\widetilde{\Lambda}^{(ij)}_{\alpha\beta} \equiv \int d\widehat{\boldsymbol{\sigma}} \left\{ \widehat{I}^{(2)}_{ij,\alpha}(\widehat{\boldsymbol{\sigma}})\widehat{\sigma}_\beta + \widehat{I}^{(2)}_{ij,\beta}(\widehat{\boldsymbol{\sigma}})\widehat{\sigma}_\alpha \right.$$
$$\left. + \frac{\epsilon_j}{\epsilon_i+\epsilon_j}\left[\widetilde{I}^{(2)}_{ij,\alpha}(\widehat{\boldsymbol{\sigma}})\widehat{\sigma}_\beta + \widetilde{I}^{(2)}_{ij,\beta}(\widehat{\boldsymbol{\sigma}})\widehat{\sigma}_\alpha\right] - \frac{m_{ij}}{m_i}(1+e_{ij})\widetilde{I}^{(3)}_{ij}(\widehat{\boldsymbol{\sigma}})\widehat{\sigma}_\alpha\widehat{\sigma}_\beta \right\}. \tag{B15}$$

Let us go further by integrating over $\widehat{\boldsymbol{\sigma}}$. Here, the following results are needed:

$$\int d\widehat{\boldsymbol{\sigma}}\Theta(\widehat{\boldsymbol{\sigma}}\cdot\boldsymbol{g})(\widehat{\boldsymbol{\sigma}}\cdot\boldsymbol{g})^n\widehat{\boldsymbol{\sigma}} = \beta_{n+1}g^{n-1}\boldsymbol{g}, \tag{B16}$$

$$\int d\widehat{\boldsymbol{\sigma}}\Theta(\widehat{\boldsymbol{\sigma}}\cdot\boldsymbol{g})(\widehat{\boldsymbol{\sigma}}\cdot\boldsymbol{g})^n\widehat{\sigma}_\alpha\widehat{\sigma}_\beta = \frac{\beta_n}{n+3}g^{n-2}(ng_\alpha g_\beta + g^2\delta_{\alpha\beta}), \tag{B17}$$

with

$$\beta_n = \pi\frac{\Gamma\left(\frac{n+1}{2}\right)}{\Gamma\left(\frac{n+3}{2}\right)} = \frac{2\pi}{n+1}. \tag{B18}$$

With the aid of Eqs. (B16)–(B17), one gets

$$\int d\widehat{\boldsymbol{\sigma}}\widehat{I}^{(2)}_{ij,\alpha}(\widehat{\boldsymbol{\sigma}})\widehat{\sigma}_\beta = \frac{\beta_3}{\pi^{3/2}(\epsilon_i+\epsilon_j)^{3/2}}\int d\boldsymbol{g}gg_\beta\exp\left(-\frac{\epsilon_i\epsilon_j}{\epsilon_i+\epsilon_j}g^2\right)\mathcal{Q}_{1,\alpha}(\{g\})$$
$$= \frac{2\sqrt{\pi}}{3}(\epsilon_i\epsilon_j)^{-3/2}\frac{1}{\sqrt{\epsilon_i\epsilon_j(\epsilon_i+\epsilon_j)}}\left(\Pi^{(i)}_{\alpha\beta} - \Pi^{(j)}_{\alpha\beta}\right), \tag{B19}$$

and thence

$$\int d\widehat{\boldsymbol{\sigma}}\widehat{I}^{(2)}_{ij,\alpha}(\widehat{\boldsymbol{\sigma}})\widehat{\sigma}_\beta + \int d\widehat{\boldsymbol{\sigma}}\widehat{I}^{(2)}_{ij,\beta}(\widehat{\boldsymbol{\sigma}})\widehat{\sigma}_\alpha = \frac{2\sqrt{\pi}}{3}(\epsilon_i\epsilon_j)^{-3/2}\left(\frac{\epsilon_i+\epsilon_j}{\epsilon_i\epsilon_j}\right)^{3/2}\frac{2\epsilon_i\epsilon_j}{(\epsilon_i+\epsilon_j)^2}\left(\Pi^{(i)}_{\alpha\beta} - \Pi^{(j)}_{\alpha\beta}\right). \tag{B20}$$

Similarly, one achieves the result

$$\int d\widehat{\boldsymbol{\sigma}}\widetilde{I}^{(2)}_{ij,\alpha}(\widehat{\boldsymbol{\sigma}})\widehat{\sigma}_\beta = \frac{\beta_3}{\pi^{3/2}(\epsilon_i+\epsilon_j)^{3/2}}\int d\boldsymbol{g}ggg_\alpha g_\beta\exp\left(-\frac{\epsilon_i\epsilon_j}{\epsilon_i+\epsilon_j}g^2\right)\mathcal{P}_1(\{g\})$$
$$= \frac{2\sqrt{\pi}}{3}(\epsilon_i\epsilon_j)^{-3/2}\left(\frac{\epsilon_i+\epsilon_j}{\epsilon_i\epsilon_j}\right)^{3/2}\left[\delta_{\alpha\beta} + \frac{6}{5}\left(\frac{\epsilon_j}{\epsilon_i+\epsilon_j}\Pi^{(i)}_{\alpha\beta} + \frac{\epsilon_i}{\epsilon_i+\epsilon_j}\Pi^{(j)}_{\alpha\beta}\right)\right], \tag{B21}$$

and then

$$\int d\widehat{\boldsymbol{\sigma}}\frac{\epsilon_j}{\epsilon_i+\epsilon_j}\left[\widetilde{I}^{(2)}_{ij,\alpha}(\widehat{\boldsymbol{\sigma}})\widehat{\sigma}_\beta + \widetilde{I}^{(2)}_{ij,\beta}(\widehat{\boldsymbol{\sigma}})\widehat{\sigma}_\alpha\right]$$
$$= \frac{2\sqrt{\pi}}{3}(\epsilon_i\epsilon_j)^{-3/2}\left(\frac{\epsilon_i+\epsilon_j}{\epsilon_i\epsilon_j}\right)^{3/2}\frac{2\epsilon_j}{\epsilon_i+\epsilon_j}\left[\delta_{\alpha\beta} + \frac{6}{5}\left(\frac{\epsilon_j}{\epsilon_i+\epsilon_j}\Pi^{(i)}_{\alpha\beta} + \frac{\epsilon_i}{\epsilon_i+\epsilon_j}\Pi^{(j)}_{\alpha\beta}\right)\right]. \tag{B22}$$

In addition, one gets

$$\int d\widehat{\boldsymbol{\sigma}}\widetilde{I}^{(3)}_{ij}(\widehat{\boldsymbol{\sigma}})\widehat{\sigma}_\alpha\widehat{\sigma}_\beta = \frac{\beta_3}{6\pi^{3/2}(\epsilon_i+\epsilon_j)^{3/2}}\int d\boldsymbol{g}(g^3\delta_{\alpha\beta} + 3gg_\alpha g_\beta)\exp\left(-\frac{\epsilon_i\epsilon_j}{\epsilon_i+\epsilon_j}g^2\right)\mathcal{P}_1(\{g\})$$
$$= \frac{2\sqrt{\pi}}{3}(\epsilon_i\epsilon_j)^{-3/2}\left(\frac{\epsilon_i+\epsilon_j}{\epsilon_i\epsilon_j}\right)^{3/2}\left[\delta_{\alpha\beta} + \frac{3}{5}\left(\frac{\epsilon_j}{\epsilon_i+\epsilon_j}\Pi^{(i)}_{\alpha\beta} + \frac{\epsilon_i}{\epsilon_i+\epsilon_j}\Pi^{(j)}_{\alpha\beta}\right)\right], \tag{B23}$$

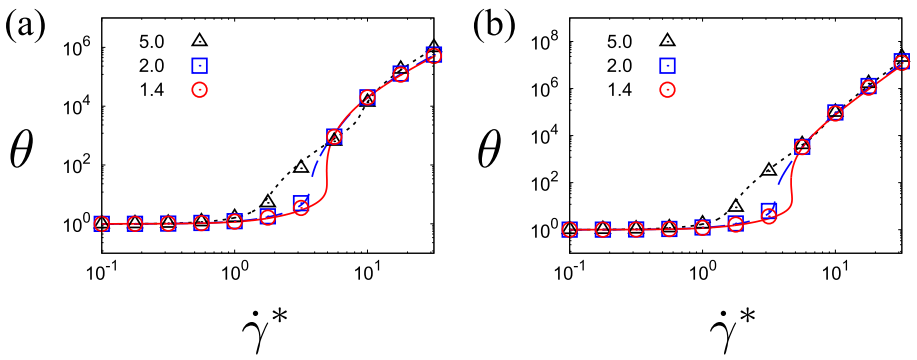

Fig. C1. (a) Dimensionless temperature θ against the dimensionless shear rate $\dot{\gamma}^*$ for $\sigma^{(1)}/\sigma^{(2)} = 1.4$ (solid line and open circles), 2.0 (dashed line and open squares), and 5.0 (dotted line and open triangles), when we fix $\varphi = 0.01$, $\xi_{\rm env} = 1.0$, and $\nu_1 = \nu_2 = 1/2$ for $e = 0.9$. (b) θ against $\dot{\gamma}^*$ for $\sigma^{(1)}/\sigma^{(2)} = 1.4$, 2.0, and 5.0 by fixing $\varphi = 0.01$, $\xi_{\rm env} = 1.0$, and $\nu_1 = \nu_2 = 1/2$ for $e = 1.0$. The lines and symbols correspond to the steady solutions of the theoretical predictions (48) and the simulation results, respectively.

and then

$$\int d\widehat{\boldsymbol{\sigma}} \frac{m_{ij}}{m_i}(1+e_{ij})\widetilde{I}_{ij}^{(3)}(\widehat{\boldsymbol{\sigma}})\widehat{\sigma}_\alpha\widehat{\sigma}_\beta = \frac{2\sqrt{\pi}}{3}(\epsilon_i\epsilon_j)^{-3/2}\left(\frac{\epsilon_i+\epsilon_j}{\epsilon_i\epsilon_j}\right)^{3/2}\frac{m_{ij}}{m_i}(1+e_{ij})\left[\delta_{\alpha\beta}+\frac{3}{5}\left(\frac{\epsilon_j}{\epsilon_i+\epsilon_j}\Pi_{\alpha\beta}^{(i)}+\frac{\epsilon_i}{\epsilon_i+\epsilon_j}\Pi_{\alpha\beta}^{(j)}\right)\right]. \tag{B24}$$

Substituting Eqs. (B20), (B22), and (B24) into Eq. (B15), one obtains

$$\begin{aligned}\widetilde{\Lambda}_{\alpha\beta}^{(ij)} &= \frac{2\sqrt{\pi}}{3}(\epsilon_i\epsilon_j)^{-3/2}\left(\frac{\epsilon_i+\epsilon_j}{\epsilon_i\epsilon_j}\right)^{3/2}\\ &\quad\times\left(\left[\frac{2\epsilon_j}{\epsilon_i+\epsilon_j}-\frac{m_{ij}}{m_i}(1+e_{ij})\right]\delta_{\alpha\beta}\right.\\ &\quad+\frac{2\epsilon_i\epsilon_j}{(\epsilon_i+\epsilon_j)^2}\left\{1+\frac{3}{5}\frac{\epsilon_i+\epsilon_j}{\epsilon_i}\left[\frac{2\epsilon_j}{\epsilon_i+\epsilon_j}-\frac{1}{2}\frac{m_{ij}}{m_i}(1+e_{ij})\right]\Pi_{\alpha\beta}^{(i)}\right\}\\ &\quad\left.-\frac{2\epsilon_i\epsilon_j}{(\epsilon_i+\epsilon_j)^2}\left\{1-\frac{3}{5}\frac{\epsilon_i+\epsilon_j}{\epsilon_j}\left[\frac{2\epsilon_j}{\epsilon_i+\epsilon_j}-\frac{1}{2}\frac{m_{ij}}{m_i}(1+e_{ij})\right]\Pi_{\alpha\beta}^{(j)}\right\}\right)\\ &= \frac{2\sqrt{\pi}}{3}(\epsilon_i\epsilon_j)^{-3/2}\left(\frac{\epsilon_i+\epsilon_j}{\epsilon_i\epsilon_j}\right)^{3/2}\left\{\left[\lambda_{ij}-\frac{1}{2}\frac{m_{ij}}{m_i}(1+e_{ij})\right]\delta_{\alpha\beta}\right.\\ &\quad\left.+2\frac{\epsilon_i\epsilon_j}{(\epsilon_i+\epsilon_j)^2}\left[\left(1+\frac{3}{5}\frac{\epsilon_i+\epsilon_j}{\epsilon_i}\lambda_{ij}\right)\Pi_{\alpha\beta}^{(i)}-\left(1-\frac{3}{5}\frac{\epsilon_i+\epsilon_j}{\epsilon_j}\lambda_{ij}\right)\Pi_{\alpha\beta}^{(j)}\right]\right\}.\end{aligned} \tag{B25}$$

Finally, the combination of Eqs. (B9) and (B25) yields Eq. (24).

Appendix C. Detailed flow curves

In this appendix, we present supplemental results of the rheology explained in Sect. 4 of the main text. We display the results for θ versus $\dot{\gamma}^*$ and $\eta^* \equiv -(\nu_1\Pi_{xy}^{(1)*} + \nu_2\Pi_{xy}^{(2)*})/\dot{\gamma}^*$ versus $\dot{\gamma}^*$.

When we focus on the reduced temperature θ (see Fig. C1), the effect of the bidispersity only appears around the intermediate-shear regime ($\dot{\gamma}^* \simeq 5.0$), where the discontinuous change

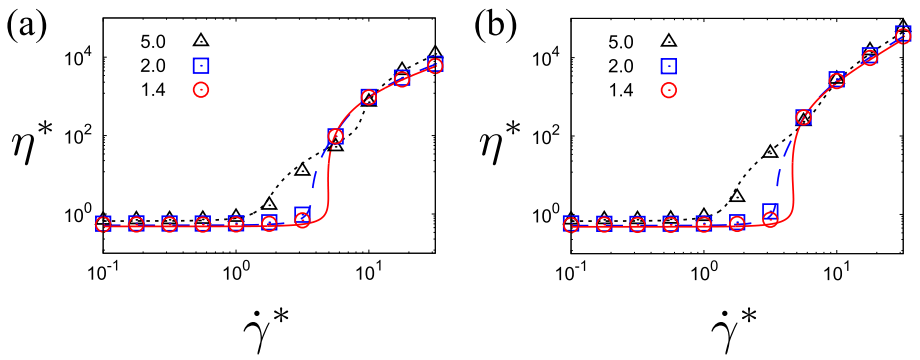

Fig. C2. The dimensionless viscosity η^* against the dimensionless shear rate $\dot{\gamma}^*$ for $\sigma^{(1)}/\sigma^{(2)} = 1.4$ (solid line and open circles), 2.0 (dashed line and open squares), and 5.0 (dotted line and open triangles) when we fix $\varphi = 0.01$, $\xi_{\rm env} = 1.0$, and $\nu_1 = \nu_2 = 1/2$ for (a) $e = 0.9$ and (b) 1. The lines and symbols correspond to the steady solutions of the theoretical predictions (49) and the simulation results, respectively.

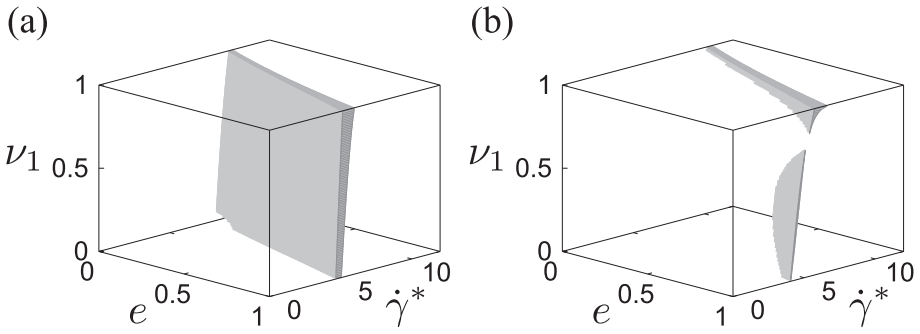

Fig. C3. Phase diagrams of the number of solutions against $(e, \nu_1, \dot{\gamma}^*)$ for (a) $\sigma^{(1)}/\sigma^{(2)} = 1.1$ and (b) 1.4 by fixing $\varphi = 0.01$ and $\xi_{\rm env} = 1.0$. Here, the filled (empty) region represents that the number of the solutions is three (unity).

corresponding to the DST is observed. Although this discontinuous change itself is reported even in monodisperse systems [13], the point at which the discontinuous change occurs depends on the size ratio. It is noteworthy that the change of the reduced temperature is drastic but continuous when the size ratio becomes large (see the data for $\sigma^{(1)}/\sigma^{(2)} = 2.0$ and 5.0 in Fig. C1).

As well as in Fig. C1, the viscosity η^* is also plotted against the shear rate $\dot{\gamma}^*$ in Fig. C2. If the size ratio $\sigma^{(1)}/\sigma^{(2)}$ is close to unity, such as 1.4, the flow curves of θ and η^* are similar to the corresponding ones for monodisperse gases, in which there are discontinuous changes of θ and η^* around $\gamma^* \approx 5$. However, as the size ratio increases, the discontinuous changes of θ and η^* become continuous. Moreover, these flow curves for inelastic inertial suspensions for large $\sigma^{(1)}/\sigma^{(2)}$ are characteristic. Indeed, the slopes of θ and η^* are oscillated with $\dot{\gamma}^*$ before reaching their asymptotic values in the large shear-rate limit.

We also draw 3D phase diagrams of the number of solutions obtained by the kinetic theory in the $(\nu_1, \dot{\gamma}^*, e)$ plane for $\varphi = 0.01$ in Fig. C3. The filled regions represent those whose number of solutions is three, while the empty regions represent only one solution. These plots show that the regions for the multiple solutions are localized in narrow regimes in the $(\nu_1, \dot{\gamma}^*, e)$ plane.

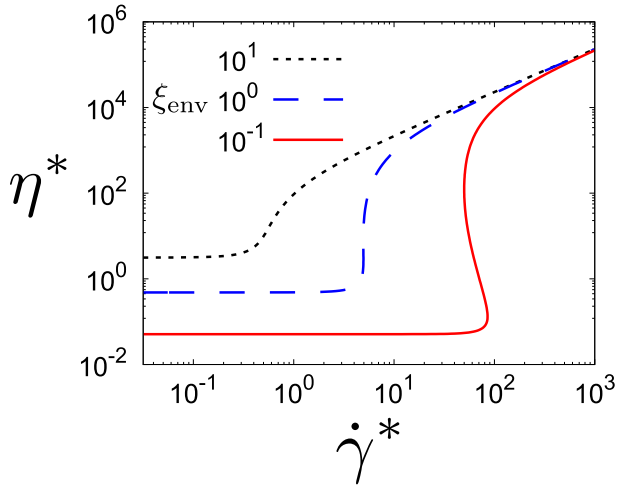

Fig. D1. Plots of the global viscosity η^* against the dimensionless shear rate $\dot{\gamma}^*$ for $\xi_{\rm env} = 10^{-1}$ (solid line), 10^0 (dashed line), and 10^1 (dotted line) when we fix $\varphi = 0.01$, $e = 0.9$, $\sigma^{(1)}/\sigma^{(2)} = 1.4$, and $\nu_1 = \nu_2 = 1/2$.

Appendix D. Appearance/disappearance of the discontinuous transition

In this appendix, let us show how the discontinuous transition appears/disappears when we change the parameters of the mixture. This appendix consists of three subsections. In the first part, we discuss how the results depend on the environmental temperature $\xi_{\rm env}$. In the second part, we distinguish the region of DST-like behavior from the CST-like behavior when we fix $\nu_1 = \nu_2 = 1/2$. In the last part, we also distinguish the region of DST-like behavior from the CST-like behavior if we fix the volume ratio $\mathcal{V} = 1$.

D.1. Effect of the environmental temperature $\xi_{\rm env}$

First, since $\xi_{\rm env} \propto \sqrt{T_{\rm env}}$, we analyze the dependence of the flow curves on the environmental temperature for $\nu_1 = \nu_2 = 1/2$. This temperature determines the state in the low-shear regime, but is independent in the high-shear regime. The latter fact is understood because interparticle collisions are dominant in the latter regime. Figure D1 illustrates the above fact: The high-shear regime is independent of the choice of environmental temperature, but the low-shear regime is determined by the value of the environmental temperature. It is interesting to note that the Newtonian regime becomes narrower as $\xi_{\rm env}$ increases. More importantly, DST-like behavior for η^* for low $\xi_{\rm env}$ becomes CST-like as $\xi_{\rm env}$ increases.

D.2. Effect of the size ratio for $N_1 = N_2$

Next, let us consider the size ratio dependence in the case of $\nu_1 = \nu_2 = 1/2$ based on the theoretical calculation. In this case, the discontinuous jumps are observed when the size ratio is not large such as $\sigma^{(1)}/\sigma^{(2)} = 1.4$ in Figs. 2 and 3 as shown in Fig. D2. On the other hand, the flow curves become continuous for larger size ratios. We can understand this behavior by considering first the discontinuous jump for the monodisperse system ($\nu_1 = 1$, $\nu_2 = 0$). Depending on the value of the (reduced) shear rate $\dot{\gamma}^* \equiv \dot{\gamma}/\zeta_1$, there are two different regimes, high-shear and low-shear regimes. The former regime is known as Bagnold's expression, $\eta^* \propto \dot{\gamma}^*/(\xi_{\rm env}^2\varphi^2)$ for $e < 1$ [13]. We note that, for the elastic case, a different expression is obtained as $\eta^* \propto \dot{\gamma}^{*2}$. However, the latter regime (low-shear regime) is determined by the interaction between the particles

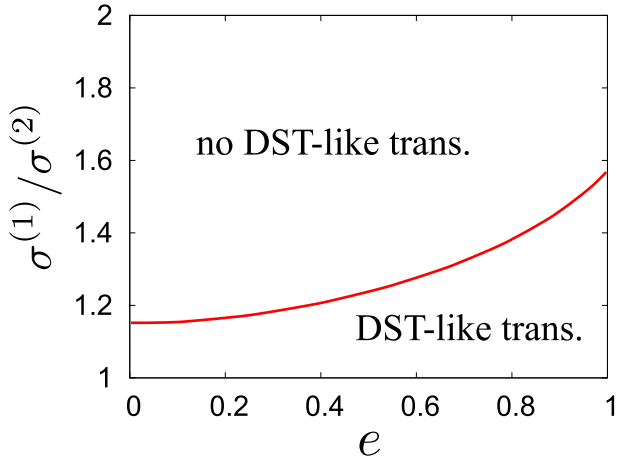

Fig. D2. Plot of the critical size ratio against the restitution coefficient when we fix $\varphi = 0.01$, $\xi_{\rm env} = 1.0$, and $\nu_1 = \nu_2 = 1/2$.

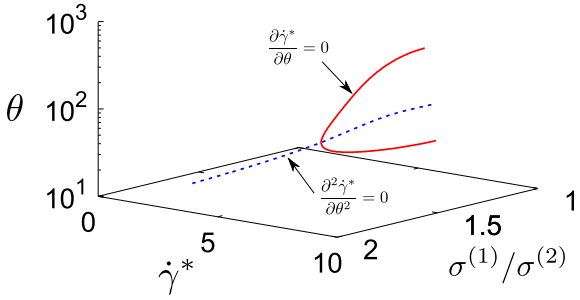

Fig. D3. Plot of the phase coexistence line $\partial\dot\gamma^*/\partial\theta = 0$ (solid lines) and the spinodal line $\partial^2\dot\gamma^*/\partial\theta^2 = 0$ (dashed line) for $\varphi = 0.01$, $e = 0.9\xi_{\rm env} = 1.0$, and $\nu_1 = \nu_2 = 1/2$.

and the solvent [13], and so $\eta^* \sim 1$. These two regimes switch to each other at $\dot\gamma^* \simeq 1$. Given that the difference between two regimes is proportional to the inverse of the volume fraction, the flow curve forms an S-shape connecting the two regimes.

Now, we consider binary systems. If the size ratio is not sufficiently large, such as $\sigma^{(1)}/\sigma^{(2)} = 1.4$ as shown in Figs. C1 and C2, the picture for the monodisperse system can also be used for a binary system. This means that the discontinuous jumps appear in this case. On the other hand, as the size ratio increases, collisions between smaller and larger particles compete with those between particles with the same size. This means that we need to discuss the mixing energy between smaller and larger particles in this case. Relating to this, we may use a discussion analogous to the phase coexistence and spinodal lines at equilibrium phase transitions, respectively, in the phase space of $(\theta, \dot\gamma^*, \sigma^{(1)}/\sigma^{(2)})$. Figure D3 shows both lines for $\varphi = 0.01$, $e = 0.9$, $\xi_{\rm env} = 1.0$, and $\nu_1 = \nu_2 = 1/2$, where the critical point is given by $\theta_{\rm c} \simeq 34.8$, $\dot\gamma^*_{\rm c} \simeq 4.81$, and $(\sigma^{(1)}/\sigma^{(2)})_{\rm c} \simeq 1.46$. This means that two (ignited and quenched) states can coexist for $\sigma^{(1)}/\sigma^{(2)} \lesssim 1.46$. This result is quite analogous to the transition from DST-like to CST-like behaviors for monodisperse cases [15].

D.3. Effect of the size ratio for $N_1 \neq N_2$

Let us consider the case of constant volume ratio $\mathcal{V} = 1$. As shown in Fig. 6, the discontinuous transition occurs as the fraction ν_1 decreases; i.e., the size ratio increases. This transition

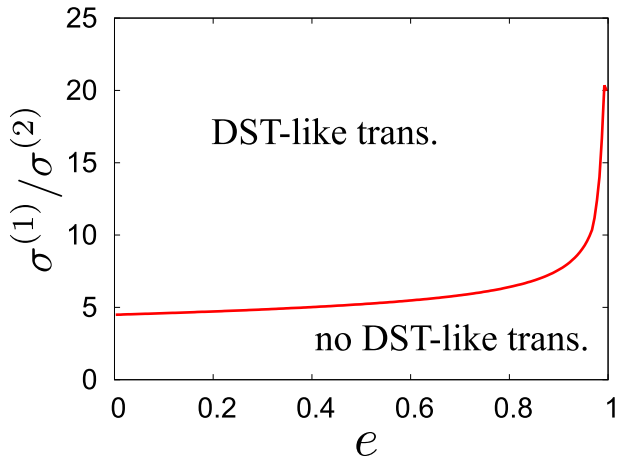

Fig. D4. Plot of the critical size ratio against the restitution coefficient e when we fix $\varphi = 0.01$, $\xi_{\rm env} = 1.0$, and $\mathcal{V} = 1$.

is different from the one found in Appendix D.2. Figure D4 plots the critical line between the discontinuous transition and continuous transition for $\varphi = 0.01$, $\xi_{\rm env} = 1.0$, and $\mathcal{V} = 1$ based on the theoretical calculation. As the restitution coefficient e increases, the minimum size ratio also increases, which means that the fraction ν_1 decreases as $\nu_1 = 1/[1 + (\sigma^{(1)}/\sigma^{(2)})^3]$ from the definition of the volume ratio $\mathcal{V}$. Unfortunately, it is a tough job to check this behavior in simulations. When the DST-like transition occurs, one needs to simulate a situation where multiple collisions between large particles occur. However, as the size ratio increases, the fraction of the larger particles, ν_1, becomes small, and the collision frequency between them also decreases. This means that the time for multiple collisions exceeds the limit of realistic simulation time.

Appendix E. Detailed analysis in the tracer limit and the finite-size effect of the simulation results

In this appendix, we display explicit expressions for the partial pressure tensors of a binary mixture in the tracer limit. These expressions are then compared with the simulation results when the number of particles is small.

In the tracer limit ($\nu_1 \to 0$), the kinetic equation for the velocity distribution function f_2 of the excess granular gas 2 is the (closed) nonlinear Boltzmann equation since its state is not perturbed by the presence of the tracer particles 1. This means that collisions between tracer and gas particles in the kinetic equation for $P^{(2)}_{\alpha\beta}$ can be neglected, i.e., $\Lambda^{(21)}_{\alpha\beta} + \Lambda^{(22)}_{\alpha\beta} \to \Lambda^{(22)}_{\alpha\beta}$ in Eq. (15) for $i = 2$. In addition, since the concentration of tracer particles is negligible, one can also neglect the tracer–tracer collisions in the kinetic equation for $P^{(1)}_{\alpha\beta}$. This implies that $\Lambda^{(11)}_{\alpha\beta} + \Lambda^{(12)}_{\alpha\beta} \to \Lambda^{(12)}_{\alpha\beta}$ in Eq. (15) for $i = 1$.

The expressions of the (reduced) elements of the pressure tensor $\Pi^{(2)}_{\alpha\beta}$ coincide with those obtained for a monodisperse granular suspension. The nontrivial components of $\Pi^{(2)}_{\alpha\beta}$ are given by [13]

$$\Pi^{(2)}_{yy} = -\frac{\lambda^{(2)*}_\eta \sqrt{\theta_2} + 2\left(1 - \theta_2^{-1}\right)}{\nu^{(2)*}_\eta \sqrt{\theta_2} + 2}, \tag{E1}$$

$$\Pi_{xy}^{(2)} = -\frac{2\theta_2^{-1} - \left(\lambda_\eta^{(2)*} - \nu_\eta^{(2)*}\right)\sqrt{\theta_2}}{\left(\nu_\eta^{(2)*}\sqrt{\theta_2} + 2\right)^2}\widetilde{\dot{\gamma}}, \tag{E2}$$

where $\widetilde{\dot{\gamma}} = \dot{\gamma}/\zeta_2$ and we have introduced

$$\lambda_\eta^{(2)*} \equiv \frac{8}{\sqrt{\pi}}\left(1 - e_{22}^2\right)\varphi_2\sqrt{\frac{T_{\rm env}}{m_2\sigma^{(2)2}\zeta_2}}, \tag{E3}$$

$$\nu_\eta^{(2)*} \equiv \frac{24}{5\sqrt{\pi}}(1 + e_{22})(3 - e_{22})\varphi_2\sqrt{\frac{T_{\rm env}}{m_2\sigma^{(2)2}\zeta_2}}, \tag{E4}$$

with the partial volume fraction

$$\varphi_2 \equiv \frac{\pi}{6}n\nu_2\sigma^{(2)3}. \tag{E5}$$

Here, it should be noted that the global temperature is approximately given by $\theta \simeq \theta_2$ in the tracer limit [26]. Using the same procedure as in Ref. [13], the reduced shear rate $\dot{\gamma}^*$ is written in terms of the reduced temperature θ_2 as

$$\dot{\gamma}^* = \left(\nu_\eta^{(2)*}\sqrt{\theta_2} + 2\right)\sqrt{\frac{3}{2}\frac{\lambda_\eta^{(2)*}\sqrt{\theta_2} + 2(1 - \theta_2^{-1})}{\left(\nu_\eta^{(2)*} - \lambda_\eta^{(2)*}\right)\sqrt{\theta_2} + 2\theta_2^{-1}}}. \tag{E6}$$

Now, let us calculate the quantities for the tracer species 1. First, the quantities $\widetilde{\Lambda}_{\alpha\alpha}^{(12)}$, $\widetilde{\Lambda}_{xy}^{(12)}$, and $\widetilde{\Lambda}_{xy}^{\prime(12)}$ are written as

$$\widetilde{\Lambda}_{\alpha\alpha}^{(12)} \equiv \frac{1}{m_2^{*3/2}}(\vartheta' + 1)^{1/2}\left\{\left[m_1^* + \frac{1}{2}m_2^*(1 - e_{12})\right]\vartheta' - \frac{1}{2}m_2^*(1 + e_{12})\right\}, \tag{E7a}$$

$$\widetilde{\Lambda}_{xy}^{(12)} \equiv \frac{1}{10m_1^*m_2^{*1/2}}\frac{1}{\theta_2(\vartheta' + 1)^{1/2}}\left[2(5 + 6\vartheta') - 3\mu_{21}(\vartheta' + 1)(1 + e_{12})\right], \tag{E7b}$$

$$\widetilde{\Lambda}_{xy}^{\prime(12)} \equiv \frac{1}{10m_2^{*3/2}}\frac{\theta_2^{-1}}{(\vartheta' + 1)^{1/2}}\left[3\mu_{21}(\vartheta' + 1)(1 + e_{12}) - 2\vartheta'\right], \tag{E7c}$$

where we have introduced $\vartheta' \equiv m_2\theta_1/(m_1\theta_2)$. Then, the nonzero elements of $\Pi_{\alpha\beta}^{(1)}$ read

$$\Pi_{xy}^{(1)} = \frac{3}{\dot{\gamma}^*\theta_1}\left[\zeta_1^*(1 - \theta_1) - \frac{1}{2}C_{12}\widetilde{\Lambda}_{\alpha\alpha}^{(12)}\theta_2^{3/2}\right], \tag{E8}$$

$$\Pi_{xx}^{(1)} = -2\Pi_{yy}^{(1)}, \tag{E9}$$

$$\Pi_{yy}^{(1)} = \Pi_{zz}^{(1)} = -\left(1 + \frac{2}{\dot{\gamma}^*}\zeta_1^*\Pi_{xy}^{(1)}\right) - 2\frac{C_{12}}{\dot{\gamma}^*}\theta_2^{3/2}\left[\widetilde{\Lambda}_{xy}^{(12)}\theta_1\Pi_{xy}^{(1)} - \widetilde{\Lambda}_{xy}^{\prime(12)}\theta_2\Pi_{xy}^{(2)}\right]. \tag{E10}$$

Substituting Eqs. (E8)–(E10) into Eq. (39a) with $C_{11} = 0$, we can obtain the equation that determines θ_1 as

$$\frac{2}{3}\dot{\gamma}^*\theta_1\Pi_{xy}^{(1)} = 2\zeta_1^*(1 - \theta_1) - C_{12}\widetilde{\Lambda}_{\alpha\alpha}^{(12)}\theta_2^{3/2}. \tag{E11}$$

Figure E1 presents the shear-rate dependence of both the temperature ratio ϑ and the viscosity ratio η_1/η_2 in the tracer limit. It should be noted that the flow curves become smooth in the whole range of the shear rate even for a larger size ratio.

The limitation of the tracer limit is also understood in Fig. E2, where the absolute values of the ratio $\left|\Lambda_{\alpha\alpha}^{(ij)}/\Lambda_{\alpha\alpha}^{(22)}\right|$ are plotted as a function of the dimensionless shear rate. Here, the

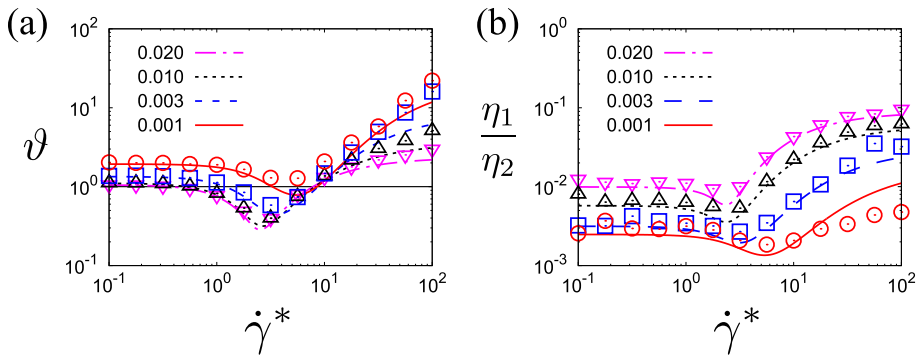

Fig. E1. (a) Temperature ratio ϑ and (b) viscosity ratio η_1/η_2 against the dimensionless shear rate $\dot{\gamma}^*$ in the tracer limit for the same set of parameters as in Fig. 5. The simulation data are obtained for $N = 1000$.

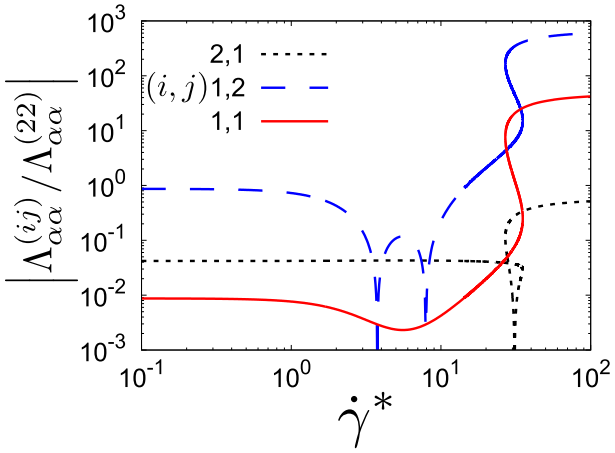

Fig. E2. Plot of $\left|\Lambda_{\alpha\alpha}^{(ij)}/\Lambda_{\alpha\alpha}^{(22)}\right|$ for $(i, j) = (1, 1)$ (solid line), $(1, 2)$ (dashed line), and $(2, 2)$ (dotted line) against the dimensionless shear rate $\dot{\gamma}^*$ for $\varphi = 0.01$, $\xi_{\rm env} = 1.0$, $e = 0.9$, $\mathcal{V} = 1$, and $\nu_1 = 1.0 \times 10^{-3}$.

expression of $\Lambda_{\alpha\alpha}^{(ij)}$ is given by Eq. (24). In the low-shear regime, the values for $(i, j) = (1, 1)$ and $(2, 1)$ are smaller than unity, which means that the contributions coming from the collisions between the large tracer particles are negligible. This indicates that the tracer limit description is a reasonable approximation in this regime. In the high-shear regime, on the other hand, the contributions from the collisions between tracer particles play an important role in the flow curve, though the number of collisions is small. Moreover, it is interesting that $\Lambda_{\alpha\alpha}^{(2,1)}$ and $\Lambda_{\alpha\alpha}^{(1,2)}$ become negative in the high- and intermediate-shear regimes, respectively, though their origins are not clear. As the number of particles used in the simulation increases, the simulation results recover the values of ϑ and η_1/η_2 in the high-shear regime. Then, we expect that the results of simulation for $N \to \infty$ agree with the theoretical results. In other words, the results of EDLSHS containing a small number of particles are not reliable in this regime.

Appendix F. 2D velocity distribution function of the BGK model

A possible way of overcoming the mathematical difficulties associated with the Boltzmann collision operators $J_{ij}[f_i, f_j]$ is to use a kinetic model. As usual, the idea behind a kinetic model is to replace the true operator J_{ij} by a simpler term that retains the main physical properties

of the above operator. In the case of dilute granular mixtures, a BGK-like kinetic model was proposed in Ref. [63]. In the case of the USF state (where $\boldsymbol{U}_1 = \boldsymbol{U}_2 = \boldsymbol{U}$), the BGK-like model is obtained by the replacement of the Boltzmann collision operator $J_{ij}[f_i, f_j]$ by the diffusive term

$$J_{ij}[\boldsymbol{V}|f_i, f_j] \to -\frac{1+e_{ij}}{2\tau_{ij}}(f_i - f_{ij}) + \frac{\varepsilon_{ij}}{2}\frac{\partial}{\partial \boldsymbol{V}}\cdot(\boldsymbol{V} f_i), \tag{F1}$$

where we have introduced the quantities

$$\frac{1}{\tau_{ij}} = \frac{8\sqrt{\pi}}{3} n_j \sigma^{(ij)2}\left(\frac{2T_i}{m_i} + \frac{2T_j}{m_j}\right)^{1/2}, \tag{F2}$$

$$\varepsilon_{ij} = \frac{1}{2\tau_{ij}}\frac{m_{ij}^2}{m_i^2}\left(1 + \frac{m_i T_j}{m_j T_i}\right)(1 - e_{ij}^2), \tag{F3}$$

$$f_{ij}(\boldsymbol{V}) = n_i\left(\frac{m_i}{2\pi T_{ij}}\right)^{3/2}\exp\left(-\frac{m_i V^2}{2T_{ij}}\right), \tag{F4}$$

$$T_{ij} = T_i + \frac{2m_i m_j}{(m_i+m_j)^2}(T_j - T_i). \tag{F5}$$

The corresponding BGK-like equation for the distribution f_1 in the steady USF is

$$-\dot{\gamma} V_y \frac{\partial f_1}{\partial V_x} - \zeta_1 \frac{\partial}{\partial \boldsymbol{V}}\cdot(\boldsymbol{V} f_1) - \frac{\zeta_1 T_{\rm env}}{m_1}\frac{\partial^2 f_1}{\partial V^2} = -\frac{1}{2}\sum_{j=1}^{2}\left[\frac{1+e_{1j}}{\tau_{1j}}(f_1 - f_{1j}) - \varepsilon_{1j}\frac{\partial}{\partial \boldsymbol{V}}\cdot(\boldsymbol{V} f_1)\right]. \tag{F6}$$

The kinetic equation for f_2 is obtained from Eq. (F6) by setting 1↔2. So far, we have not been able to obtain the explicit exact form of $f_i(\boldsymbol{V})$ in Eq. (F6). An exception corresponds to the simple limit case $T_{\rm env} = 0$ with keeping $\zeta_i = {\rm const}$. This corresponds to a situation where the background temperature $T_{\rm env}$ is much smaller than the kinetic temperature T under the high-shear-rate limit. Hence, the suspension model ignores the effects of thermal fluctuations on solid particles and the impact of the gas phase on grains is only accounted for by the drag force term. Although ζ_i should be proportional to $\sqrt{T_{\rm env}}$ for hard-core molecules, such a simplified model has been employed in some previous works [9,10,14].

If we take the limit $T_{\rm env}/T \ll 1$, Eq. (F6) becomes

$$-\dot{\gamma} V_y \frac{\partial f_1}{\partial V_x} - 3\alpha_1 f_1 - \alpha_1 \boldsymbol{V}\cdot\frac{\partial f_1}{\partial \boldsymbol{V}} + \xi_1 f_1 = \Phi_1, \tag{F7}$$

where we have introduced the parameters:

$$\alpha_1 = \zeta_1 + \frac{\varepsilon_{11} + \varepsilon_{22}}{2}, \tag{F8}$$

$$\xi_1 = \frac{1}{2}\left(\frac{1+e_{11}}{\tau_{11}} + \frac{1+e_{12}}{\tau_{12}}\right), \tag{F9}$$

$$\Phi_1 = \frac{1}{2}\left(\frac{1+e_{11}}{\tau_{11}} f_{11} + \frac{1+e_{12}}{\tau_{12}} f_{12}\right). \tag{F10}$$

The formal solution of Eq. (F7) can be written as

$$\begin{aligned} f_1(\boldsymbol{V}) &= \left(\xi_1 - 3\alpha_1 - \dot{\gamma} V_y \frac{\partial}{\partial V_x} - \alpha_1 \boldsymbol{V}_1\cdot\frac{\partial}{\partial \boldsymbol{V}_1}\right)^{-1}\Phi_1(\boldsymbol{V}) \\ &= \int_0^\infty ds\, e^{-(\xi_1 - 3\alpha_1)s} e^{\dot{\gamma} s V_y \frac{\partial}{\partial V_x}} e^{\alpha_1 s \boldsymbol{V}\cdot\frac{\partial}{\partial \boldsymbol{V}}}\Phi_1(\boldsymbol{V}). \end{aligned} \tag{F11}$$

Note that the velocity operators appearing in Eq. (F11) commute. Their action on an arbitrary function $g(\boldsymbol{V}) \equiv g(V_x, V_y, V_z)$ is

$$e^{\dot{\gamma} s V_y \frac{\partial}{\partial V_x}} g(\boldsymbol{V}) = g(V_x + \dot{\gamma} s V_y, V_y, V_z), \tag{F12a}$$

$$e^{\alpha_1 s \boldsymbol{V} \cdot \frac{\partial}{\partial \boldsymbol{V}}} g(\boldsymbol{V}) = g\left(e^{\alpha_1 s} \boldsymbol{V}\right). \tag{F12b}$$

Taking into account the action of these operators in Eq. (F11), the velocity distribution $f_1(\boldsymbol{V})$ can be written as

$$f_1(\boldsymbol{V}) = n_1 \left(\frac{m_1}{2T_1}\right)^{3/2} g_{1,\mathrm{B}}(\boldsymbol{c}), \quad \boldsymbol{c} \equiv \left(\frac{m_1}{2T_1}\right)^{-1/2} \boldsymbol{V}, \tag{F13}$$

where

$$\begin{aligned} g_{1,\mathrm{B}}(\boldsymbol{c}) &= \pi^{-3/2} \int_0^\infty ds\, e^{-(\xi_1 - 3\alpha_1)s} \left\{ \frac{1+e_{11}}{2\tau_{11}} \chi_1^{-3/2} \exp\left[-\chi_1^{-1} e^{2\alpha_1 s} \left((c_x + \dot{\gamma} s c_y)^2 + c_y^2 + c_z^2\right)\right] \right. \\ &\quad \left. + \frac{1+e_{12}}{2\tau_{12}} \chi_{12}^{-3/2} \exp\left[-\chi_{12}^{-1} e^{2\alpha_1 s} \left((c_x + \dot{\gamma} s c_y)^2 + c_y^2 + c_z^2\right)\right] \right\} \\ &= \pi^{-3/2} \int_0^\infty ds\, e^{-(\xi_1^* - 3\alpha_1^*)s} \left\{ \frac{1+e_{11}}{2\tau_{11}^*} \chi_1^{-3/2} \exp\left[-\chi_1^{-1} e^{2\alpha_1^* s} \left((c_x + \dot{\gamma}^* s c_y)^2 + c_y^2 + c_z^2\right)\right] \right. \\ &\quad \left. + \frac{1+e_{12}}{2\tau_{12}^*} \chi_{12}^{-3/2} \exp\left[-\chi_{12}^{-1} e^{2\alpha_1^* s} \left((c_x + \dot{\gamma}^* s c_y)^2 + c_y^2 + c_z^2\right)\right] \right\}. \end{aligned} \tag{F14}$$

Here, $\xi_1^* \equiv \xi_1 \overline{\sigma}/\sqrt{\overline{m}/T_{\mathrm{env}}}$, $\alpha_1^* \equiv \alpha_1 \overline{\sigma}/\sqrt{\overline{m}/T_{\mathrm{env}}}$, $\tau_{ij}^* \equiv \tau_{ij}\sqrt{T_{\mathrm{env}}/\overline{m}}/\overline{\sigma}$, $\chi_1 \equiv T_1/T$, and $\chi_{12} \equiv T_{12}/T$.

To illustrate the shear-rate dependence of the BGK distribution $g_{1,\mathrm{B}}(\boldsymbol{c})$, let us define the marginal (2D) distribution function:

$$g_{1,\mathrm{B}}^{(xy)}(c_x, c_y) = \int_{-\infty}^\infty dc_z g_{1,\mathrm{B}}(\boldsymbol{c}). \tag{F15}$$

From Eq. (F14), one gets

$$\begin{aligned} g_{1,\mathrm{B}}^{(xy)}(c_x, c_y) &= \frac{1}{\pi} \int_0^\infty ds\, e^{-(\xi_1^* - 2\alpha_1^*)s} \left\{ \frac{1+e_{11}}{2\tau_{11}^*} \chi_1^{-1} \exp\left[-\chi_1^{-1} e^{2\alpha_1^* s} \left((c_x + \dot{\gamma} s c_y)^2 + c_y^2\right)\right] \right. \\ &\quad \left. + \frac{1+e_{12}}{2\tau_{12}^*} \chi_{12}^{-1} \exp\left[-\chi_{12}^{-1} e^{2\alpha_1^* s} \left((c_x + \dot{\gamma} s c_y)^2 + c_y^2\right)\right] \right\}. \end{aligned} \tag{F16}$$

Figure 11 shows how this model works when we compare it with the simulation results. Interestingly, the BGK-like model gives the correct VDF in the wider range of the (c_x, c_y) plane in the high-shear regime. In particular, some features of the true VDF (such as the enhancement in the shear direction and the form of $g_1^{(xy)}$ near the positive and negative peaks) are captured in a more precise way by the BGK distribution compared to Grad's distribution (see Figs. 9 and 11). Nevertheless, we recall that the applicability of the solution (F16) to the BGK-like model is limited to the high-shear regime. As the environmental temperature plays a role in the rheology, the BGK solution (F16) cannot capture the properties of the VDF in the complete range of shear rates [see Figs. 11(a), (b), and (c)].

Appendix G. 1D velocity distribution function

In the main text and Appendix F, we have compared the marginal 2D velocity distribution function obtained from the simulations with those obtained from Grad's method and the BGK-

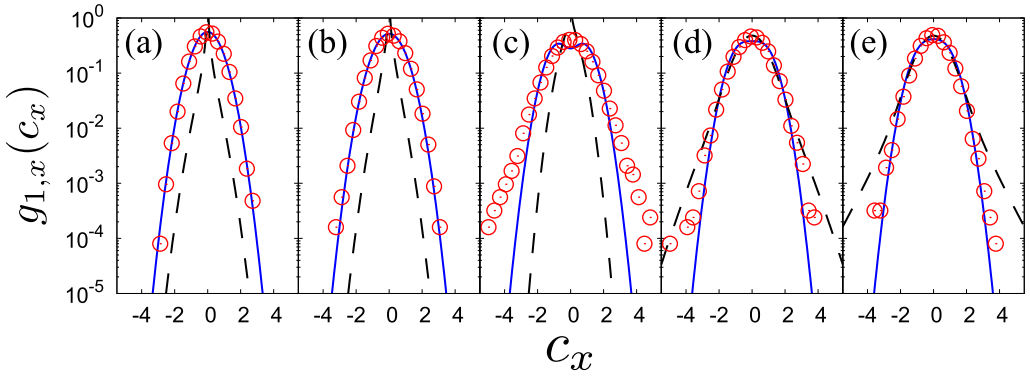

Fig. G1. 1D velocity distribution functions of the larger particles for (a) $\dot{\gamma}^* = 0.32$, (b) 1.0, (c) 3.2, (d) 10, and (e) 32 when we fix $\varphi = 0.01$, $e = 0.9$, $\xi_{\rm env} = 1.0$, and $\sigma^{(1)}/\sigma^{(2)} = 2.0$. The solid and dashed lines represent Grad's approximation (G1) and the BGK model (G2), respectively.

like model. In this appendix, on the other hand, we investigate whether both approximations work when we consider the 1D velocity distribution.

Let us define the marginal (1D) distribution obtained from Grad's method:

$$g_{1,\mathrm{G}}^{(x)}(c_x) \equiv \int_{-\infty}^{\infty} dc_y g_{1,\mathrm{G}}^{(xy)}(c_x, c_y) = \frac{1}{\sqrt{\pi}} e^{-c_x^2} \left(1 - \frac{\Pi_{xx}^{(1)}}{2} + \Pi_{xx}^{(1)} c_x^2\right), \tag{G1}$$

and from the BGK model:

$$\begin{aligned} g_{1,\mathrm{B}}^{(x)}(c_x) &\equiv \int_{-\infty}^{\infty} dc_y g_{1,\mathrm{B}}^{(xy)}(c_x, c_y) \\ &= \frac{1}{\sqrt{\pi}} \int_0^{\infty} ds \frac{e^{-(\xi_1^* - \alpha_1^*)s}}{\sqrt{1 + \dot{\gamma}^{*2} s^2}} \left[\frac{1 + e_{11}}{2\tau_{11}^*} \chi_1^{-1/2} \exp\left(-\chi_1^{-1} e^{2\alpha_1^* s} \frac{c_x^2}{1 + \dot{\gamma}^{*2} s^2}\right)\right. \\ &\quad \left. + \frac{1 + e_{12}}{2\tau_{12}^*} \chi_{12}^{-1/2} \exp\left(-\chi_{12}^{-1} e^{2\alpha_1^* s} \frac{c_x^2}{1 + \dot{\gamma}^{*2} s^2}\right)\right]. \end{aligned} \tag{G2}$$

Figure G1 shows a comparison of the VDF obtained from the simulations with Eqs. (G1) and (G2) when we control the shear rate from $\dot{\gamma}^* = 0.32$ to 32. Here, we have fixed $\varphi = 0.01$, $e = 0.9$, $\xi_{\rm env} = 1.0$, and $\sigma^{(1)}/\sigma^{(2)} = 2.0$. The 1D VDF estimated from Grad's method works well in the wide range of the shear rate, although this approximation cannot reproduce the fat tail of the VDF in the intermediate regime. The consistency in the high-shear regime is different when we compare it with the 2D VDF in Figs. 9(c), (d), and (e). On the other hand, the BGK 1D VDF is worse than that of Grad's distribution. Although it captures the behavior of the VDF near $c_x \sim 0$, the solution to the BGK-like model overestimates the high-energy tail of the VDF in the high-shear regime [see Figs. G1(d) and (e)].

References

[1] H. A. Barnes, J. Rheol. **33**, 329 (1989).
[2] J. Mewis and N. J. Wagner, Colloidal Suspension Rheology (Cambridge University Press, New York, 2011).
[3] M. Otsuki and H. Hayakawa, Phys. Rev. E **83**, 051301 (2011).
[4] R. Seto, R. Mari, J. F. Morris, and M. M. Denn, Phys. Rev. Lett. **111**, 218301 (2013).
[5] E. Brown and H. M. Jaeger, Rep. Prog. Phys. **77**, 040602 (2014).
[6] D. Lootens, H. van Damme, Y. Hémar, and P. Hébraud, Phys. Rev. Lett. **95**, 268302 (2005).
[7] C. D. Cwalina and N. J. Wagner, J. Rheol. **58**, 949 (2004).

[8] D. L. Koch and R. J. Hill, Ann. Rev. Fluid Mech. **33**, 619 (2001).
[9] H.-K. Tsao and D. L. Koch, J. Fluid Mech. **296**, 211 (1995).
[10] A. S. Sangani, G. Mo, H.-K. Tsao, and D. L. Koch, J. Fluid Mech. **313**, 309 (1996).
[11] M. G. Chamorro, F. Vega Reyes, and V. Garzó, Phys. Rev. E **92**, 052205 (2015).
[12] H. Hayakawa and S. Takada, EPJ Web Conf. **140**, 09003 (2017).
[13] H. Hayakawa and S. Takada, Prog. Theor. Exp. Phys. **2019**, 083J01 (2019).
[14] S. Saha and M. Alam, J. Fluid. Mech. **833**, 206 (2017).
[15] H. Hayakawa, S. Takada, and V. Garzó, Phys. Rev. E **96**, 042903 (2017); **101**, 069904(E) (2020) [erratum].
[16] S. Takada, H. Hayakawa, A. Santos, and V. Garzó, Phys. Rev. E **102**, 022907 (2020).
[17] S. Sugimoto and S. Takada, J. Phys. Soc. Jpn. **89**, 084803 (2020); **89**, 127001 (2020) [addendum].
[18] A. Scala, Phys. Rev. E **86**, 026709 (2012).
[19] G. P. Krishnan, S. Beimfohr, and D. T. Leighton, J. Fluid Mech. **321**, 371 (1996).
[20] C. Gamonpilas, J. F. Morris, and M. M. Denn, J. Rheol. **60**, 289 (2016); **62**, 665 (2018) [erratum].
[21] S. Pednekar, J. Chun, and J. F. Morris, J. Rheol. **62**, 513 (2018).
[22] Z. Liu, J. R. Clausen, R. R. Rao, and C. K. Aidun, J. Fluid Mech. **871**, 636 (2019).
[23] V. Garzó, Granular Gaseous Flows: A Kinetic Theory Approach to Granular Gaseous Flows (Springer, Cham, 2019).
[24] O. Zik and J. Stavans, Europhys. Lett. **16**, 255 (1991).
[25] N. Menon and D. J. Durian, Science **28**, 1220 (1997).
[26] V. Garzó, Phys. Rev. E **66**, 021308 (2002).
[27] V. Garzó, J. Stat. Mech. **2007**, P02012 (2007).
[28] C. S. Campbell, J. Fluid Mech. **348**, 85 (1997).
[29] A. Artoni, M. Larcher, J. T. Jenkins, and P. Richard, Soft Matter **17**, 2596 (2021).
[30] S. S. Hsiau and W. L. Yang, Phys. Fluids **14**, 612 (2002).
[31] B. Utter and R. P. Behringer, Phys. Rev. E **69**, 031308 (2004).
[32] B. Andreotti, Y. Forterre, and O. Pouliquen, Granular Media: Between Fluid and Solid (Cambridge University Press, Cambridge, 2013).
[33] J. T. Jenkins and F. Mancini, J. Appl. Mech. **109**, 27 (1987).
[34] S. Puri and H. Hayakawa, Physica A **270**, 115 (1999).
[35] J. T. Jenkins and D. Yoon, Phys. Rev. Lett. **88**, 194301 (2002).
[36] L. Trujillo, M. Alam, and H. J. Herrmann, Europhys. Lett. **64**, 190 (2003).
[37] J. M. N. T. Gray and A. R. Thornton, Proc. R. Soc. A **461**, 1447 (2005).
[38] V. Garzó, Europhys. Lett. **75**, 521 (2006).
[39] V. Garzó, Phys. Rev. E **78**, 020301(R) (2008).
[40] B. Marks, P. Rognon, and I. Einav, J. Fluid Mech. **690**, 499 (2011).
[41] J. M. N. T. Gray, Ann. Rev. Fluid Mech. **50**, 407 (2018).
[42] L. Jing, J. M. Ottino, R. M. Lueptow, and P. B. Umbanhowar, J. Fluid Mech. **925**, A29 (2021).
[43] M. Alam and S. Luding, J. Fluid Mech. **476**, 69 (2003).
[44] A. Sarracino, D. Villamaina, C. G. Costantini, and A. Puglisi, J. Stat. Mech. **2010**, P04013 (2010).
[45] N. Khalil and V. Garzó, Phys. Rev. E **88**, 052201 (2013).
[46] N. Khalil and V. Garzó, Phys. Rev. E **97**, 022902 (2018); **99**, 059901(E) (2019) [erratum].
[47] J. M. Montanero and V. Garzó, Physica A **310**, 17 (2002).
[48] J. F. Lutsko, Phys. Rev. E **70**, 061101 (2004).
[49] M. G. Chamorro and V. Garzó, Phys. Fluids **35**, 027121 (2023).
[50] V. Garzó and F. Vega Reyes, J. Stat. Mech. **2010**, P07024 (2010).
[51] D. Bi, J. Zhang, B. Chakraborty, and R. Behringer, Nature **480**, 355 (2011).
[52] A. Fall, F. Bertrand, D. Hautemayou, C. Mezière, P. Moucheront, A. Lemaître, and G. Ovarlez, Phys. Rev. Lett. **114**, 098301 (2015).
[53] I. R. Peters, S. Majumdar, and H. M. Jaeger, Nature **532**, 214 (2016).
[54] M. Otsuki and H. Hayakawa, Phys. Rev. E **101**, 032905 (2020).
[55] R. Gómez González, N. Khalil, and V. Garzó, Phys. Rev. E **101**, 012904 (2020).
[56] R. Gómez González and V. Garzó, Phys. Rev. E **106**, 064902 (2022).
[57] N. G. van Kampen, Stochastic Processes in Physics and Chemistry (North-Holland, Amsterdam, 2007), 3rd ed.
[58] H. Grad, Commun. Pure Appl. Math. **2**, 331 (1949).

[59] A. Santos, V. Garzó, and J. W. Dufty, Phys. Rev. E **69**, 061303 (2004).
[60] V. Garzó, Phys. Fluids, **25**, 043301 (2013).
[61] V. Garzó and E. Trizac, EPL **94**, 50009 (2011).
[62] V. Garzó and E. Trizac, Phys. Rev. E **85**, 011302 (2012).
[63] F. Vega Reyes, V. Garzó, and A. Santos, Phys. Rev. E **75**, 061306 (2007).